

Under-ice acoustic navigation using real-time model-aided range estimation

EeShan C. Bhatt¹,^{1,a} Oscar Viquez,¹ and Henrik Schmidt¹

*Department of Mechanical Engineering, Massachusetts Institute of Technology,
Cambridge, MA*

(Dated: 23 February 2022)

1 The long baseline (LBL) underwater navigation paradigm relies on the conversion of
2 travel times into pseudoranges to trilaterate position. For real-time operations, this
3 conversion assumes an isovelocity sound speed. For re-navigation, computationally
4 and/or labor intensive acoustic modeling may be employed to reduce uncertainty.
5 This work demonstrates a real-time ray-based prediction method of the effective
6 sound speed along a path from source to receiver to minimize pseudorange error.
7 This method was implemented for an AUV-LBL system in the Beaufort Sea, in total
8 ice-covered conditions and a double-ducted propagation environment. Given the lack
9 of GNSS data throughout the vehicle's mission, the pseudorange performance is first
10 evaluated on connections between GNSS-linked beacons. The real-time ranging error
11 between beacons is roughly 11 meters at distances up to 3 km. A consistent overes-
12 timation in the real-time method provides insights for improved eigenray filtering by
13 the number of bounces. An operationally equivalent pipeline is used to re-position
14 the LBL beacons and re-navigate the AUV, using modeled, historical, and a locally
15 observed sound speed profiles. The median re-navigation error is 1.84 ± 2.19 m.
16 The improved performance for suggests that this approach extends the single meter
17 accuracy of the deployed GNSS units into the water column.

^aebhatt@whoi.edu

¹⁸ **I. INTRODUCTION**

¹⁹ Autonomous underwater vehicles (AUVs) are increasingly capable platforms to explore
²⁰ and sample the ocean, particularly for remote and/or dangerous regions. However, navi-
²¹ gation uncertainty is a major challenge in considering AUVs as standard tools for oceano-
²² graphic research. While land and air-based robots utilize information from Global Nav-
²³ igation Satellite Systems (GNSS) to achieve single-meter location accuracy and precision
²⁴ throughout the duration of their missions, AUVs cannot access GNSS fixes while under-
²⁵ water. Therefore, underwater vehicles have relied on any combination of dead reckoning,
²⁶ hydrodynamic models, inertial navigation systems, doppler velocity logs, and acoustic base-
²⁷ line positioning systems for navigation ([Paull *et al.*, 2014](#)). Limiting navigation error and
²⁸ drift requires an AUV to periodically stall on the surface and obtain a GNSS fix to reset its
²⁹ position error. This foolproof method of self-positioning is undesirable for stealth, adverse
³⁰ weather conditions, and mission efficiency, and inaccessible in a GNSS-denied situation like
³¹ an ice-covered environment.

³² Of underwater acoustic navigation systems, long baseline (LBL) is the most GPS-like
³³ in style and scale, and most appropriate for mitigating drift without overburdening com-
³⁴ putation or payload size on the vehicle ([Van Uffelen, 2021](#)). The state-of-the-art for LBL
³⁵ outsources depth to a pressure sensor and solves the two-dimensional localization problem
³⁶ with an isovelocity, linear scaling between one way travel time (OWTT) and range ([Eustice](#)
³⁷ *et al.*, 2006, 2007; [Webster *et al.*, 2009, 2012](#)). This assumption is valid for short scale op-
³⁸ erations but oversimplifies propagation at larger scales or complex sound speed structure.

39 To achieve single meter, GNSS-like performance in a GNSS-denied environment, we demon-
 40 strate an embedded ray-based data processing algorithm to convert recorded OWTTs into
 41 pseudorange estimates. This methodology was integrated onto the AUV *Macrura*, deployed
 42 and recovered in the Beaufort Sea, in March 2020, during the Ice Exercise 2020 (ICEX20).
 43 A physics-driven methodology that received an *in situ* sound speed profile (SSP) was nec-
 44 essary despite the small operational domain because of the relatively high-risk mission en-
 45 vironment—total under-ice conditions and a variable double ducted acoustic environment.
 46 For consistency, we delineate specific definitions for timing, positioning, and navigation
 47 from [Howe et al. \(2019\)](#).

- 48 1. Timing is the ability to acquire and maintain accurate and precise time anywhere in
 the domain of interest within user-defined timeliness parameters
- 50 2. Positioning is the ability to accurately and precisely determine one's location refer-
 enced to a standard geodetic system
- 52 3. Navigation is the ability to determine current and desired position (relative or absolute)
 and apply corrections to course, orientation, and speed to attain a desired position
 anywhere in the domain of concern

55 Thus, navigation is inherently in real-time and depends on positioning; positioning depends
 56 on timing. We also suggest re-navigation and re-positioning as post-processed corollaries,
 57 which may include knowledge or processing capabilities not available *in situ*.

58 While RAFOS floats championed one way ranging for re-positioning ([Duda et al., 2006](#);
 59 [Rossby et al., 1986](#)), the ability to do so for navigation was facilitated by the advent of

60 the WHOI Micro-Modem (Singh *et al.*, 2006) and synchronized clocks (Rypkema *et al.*,
61 2017). AUV navigation efforts have achieved root mean square (RMS) localization error on
62 the order of tens of meters relative to GNSS surface position over less than ten kilometers
63 in shallow (Claus *et al.*, 2018; Eustice *et al.*, 2007; Kepper *et al.*, 2017) and deep water
64 (Jakuba *et al.*, 2008; Kunz *et al.*, 2008; Webster *et al.*, 2009). However, these efforts all used
65 a nominal sound speed for travel time conversion and the vehicles were limited to shallower
66 isovelocity regimes.

67 Localization algorithms that do consider environmental or acoustic uncertainty tend to
68 focus on longer duration and larger range experiments, where spatio-temporal variability
69 cannot be ignored. These methods have also been reserved for post-processing as they
70 can be labor intensive, computationally heavy, and/or require additional information like
71 contemporaneous data. For example, gliders navigating with kinematic flight models and
72 equipped with acoustic modems were later unambiguously associated with predicted ray
73 arrivals, resulting in roughly a kilometer error and hundred meters uncertainty over basin
74 scale propagation (Van Uffelen *et al.*, 2013). A follow up study investigated how a single
75 temporally and spatially averaged SSP could mitigate position error for a four month glider
76 mission (Van Uffelen *et al.*, 2016). Wu *et al.* (2019) cross correlate three days of real acous-
77 tic records with synthetic ones generated through ocean model snapshots from HYCOM
78 (Chassagnet *et al.*, 2007). While potentially applicable for various ocean states, this is re-
79 liant on model realism and impractical for real-time operations. A “cold start” algorithm
80 that does not require prior knowledge of track, position, or sound speed information inputs
81 a four-dimensional ocean model, constrained by tomography data, into a range dependent

82 ray code to isolate the last path detected in a full multipath pattern (Mikhalevsky *et al.*,
83 2020). Then, a representative group speed is solved for alongside position in a least squares
84 fashion. This approach is able to re-position a floating hydrophone array with an error of
85 58 m and a standard deviation of 32 m based on six sources 129–450 km away but remains
86 to seen for real-time navigation.

87 The ICEX20 AUV deployment necessitated an environmentally- and physically-driven
88 relationship between recorded travel times and estimated pseudoranges due to the multipath
89 uncertainty brought upon by an increasingly observed double ducted environment in the
90 Beaufort Sea, which some refer to as the “Beaufort Lens” (Chen *et al.*, 2019; Chen and
91 Schmidt, 2020; Litvak, 2015).

92 Given that a lens introduces significant ray refraction, the Beaufort Lens is a shorthand for
93 the spatio-temporal variability of the local temperature and sound speed maxima generally
94 around 50 to 60 m in depth. A neutrally buoyant layer of warm Pacific Summer Water
95 creates a unique double ducted environment —the upper duct degrades signal coherence
96 due to intensified ice interaction and the lower duct effectively traps sound for long range
97 propagation (Poulsen and Schmidt, 2017). Modeling output (Duda *et al.*, 2021, 2019) and
98 experimental observations (Ballard *et al.*, 2020; Bhatt, 2021) suggest that, in the Beaufort
99 Sea, the duct is persistent and widespread but not necessarily continuous; it and its acoustic
100 effects can be non-existent, minimal, or drastic. Transmissions in the upper duct, between
101 the surface ice and the lens, experience minimal attenuation but degrade in signal coherence
102 with repeated reflections under the ice. In the lower duct, between the lens and its conjugate

¹⁰³ depth in the Atlantic water (roughly 200 m), sound above 350 Hz is trapped near losslessly
¹⁰⁴ for long range propagation (Poulsen and Schmidt, 2017).

¹⁰⁵ The Arctic, while remote, is the perfect place to demonstrate mature navigation tech-
¹⁰⁶ nologies in real GNSS-denied conditions. Thorough reviews of uncrewed vehicle operations
¹⁰⁷ in polar environments can be found in Norgren *et al.* (2014) and Barker *et al.* (2020); there
¹⁰⁸ is no comparable work in the Arctic for a short range AUV deployment in the Beaufort
¹⁰⁹ Lens. Seminal Arctic AUV deployments (Bellingham *et al.*, 1995; Brooke, 1981; Hayes and
¹¹⁰ Morison, 2002; Jackson, 1983; Light and Morison, 1989) and more recent ones (Fossum
¹¹¹ *et al.*, 2021; Jakuba *et al.*, 2008; Kukulya *et al.*, 2010; Kunz *et al.*, 2008; Plueddemann *et al.*,
¹¹² 2012; Timmermans and Winsor, 2013) witnessed the classical upward refracting sound speed
¹¹³ profile that is amenable to an isovelocity assumption.

¹¹⁴ Of note, despite different platforms and scales, are recent glider deployments in the
¹¹⁵ Canada Basin. In 2014, in partially ice-covered conditions, a long range LBL system with
¹¹⁶ WHOI Micro-Modems at 100 m depth exploited the lower duct for long range communication
¹¹⁷ with two gliders (Freitag *et al.*, 2016; Webster *et al.*, 2015). The sound speed value measured
¹¹⁸ at the time of reception was used to estimate pseudorange in post-processing. The beacon-
¹¹⁹ to-beacon performance was excellent, achieving contact at ranges greater than 200 km with
¹²⁰ a position uncertainty of 40 m. The beacon-to-glider performance, however, deteriorated
¹²¹ due to missed contacts outside the duct, and was not described quantitatively. In 2017,
¹²² gliders were deployed in a region with no ice coverage (Graupe *et al.*, 2019). Ranges were
¹²³ linearly scaled by a statistical description of sound speed observations taken during the
¹²⁴ experiment, 1450 ± 6.5 m/s. This resulted in an error of 550 m, which was reduced by

125 a factor between 4 and 5, depending on the dive, using a post-processing acoustic arrival
126 matching method. Both cases exploit the lower duct for high fidelity communication at long
127 ranges. Unintuitively, the smaller scale nature of our deployment during ICEX20 is not a
128 simplifying factor. For source depths typical to vehicle operations, 30 to 200 m, the Beaufort
129 Lens introduces a shadow zone that spans from 2 to 6 kilometers in range ([Schmidt and](#)
130 [Schneider, 2016](#)).

131 Compared to previous small scale navigation efforts, the approach in this paper integrates
132 real-time model-aided data processing to estimate a representative sound speed along a path
133 from source to receiver, leveraging climatology, *in situ* data, and fast acoustic modeling. The
134 paper is organized as follows. Section [II](#) details the experimental approach and conditions
135 during ICEX20. Given that there is no GNSS ground truth for the vehicle position while
136 underway, we first evaluate the real-time ranging performance of GPS-linked beacon-to-
137 beacon communication events in section [III](#). Section [IV](#) uses insights from field data to
138 introduce a new ray filtering algorithm to improve range estimation. Section [V](#) emulates the
139 real-time processing pipeline to re-position beacon-to-beacon events and re-navigate AUV
140 *Macrura*.

¹⁴¹ **II. OVERVIEW OF THE ICEX20 EXPERIMENT**

¹⁴² The results from this paper derive from data collected while deploying the AUV *Macrura*,
¹⁴³ a custom Bluefin-21, during the Ice Exercise 2020 (ICEX20). The experiment was conducted
¹⁴⁴ in the Beaufort Sea, from March 8th to 11th, at roughly 71.2°N. The AUV deployment was
¹⁴⁵ supported by the Integrated Communication and Navigation Network (ICNN) ([Randeni et al., 2020, 2021; Schneider et al., 2021](#)) a specialized implementation of the LBL solution.
¹⁴⁶
¹⁴⁷ The ICNN was initially developed via numerous virtual experiments to ensure robust algo-
¹⁴⁸ rithms and interfaces between different hardware components. The simulation capabilities
¹⁴⁹ are largely physics-driven with a modular system of systems approach—an environmental
¹⁵⁰ simulator with sub-components for the ocean, including Arctic ice drift and ocean acoustic
¹⁵¹ propagation; a vehicle simulator with sub-components for vehicle dynamics and navigation;
¹⁵² a topside hardware simulator and acoustic communications simulator, both with a software-
¹⁵³ only configuration and a hardware-in-the-loop version ([Schneider and Schmidt, 2018](#)). The
¹⁵⁴ virtual environment similarly emulates the interfaces between the real components to test
¹⁵⁵ the entire software pipeline.

¹⁵⁶ **A. The Integrated Communication and Navigation Network**

¹⁵⁷ The ICNN is comprised of four ice buoys in a loose rectangle, roughly 2 km away from
¹⁵⁸ a central ice camp with a topside computer, as shown in Fig. 1. Each ice buoy is outfitted
¹⁵⁹ with a Garmin GPS 18x, with a pulse-per-second rising edge aligned to 1 microsecond and
¹⁶⁰ a spec sheet accuracy of 3 m, 95% of the time. They are also each equipped with a WHOI

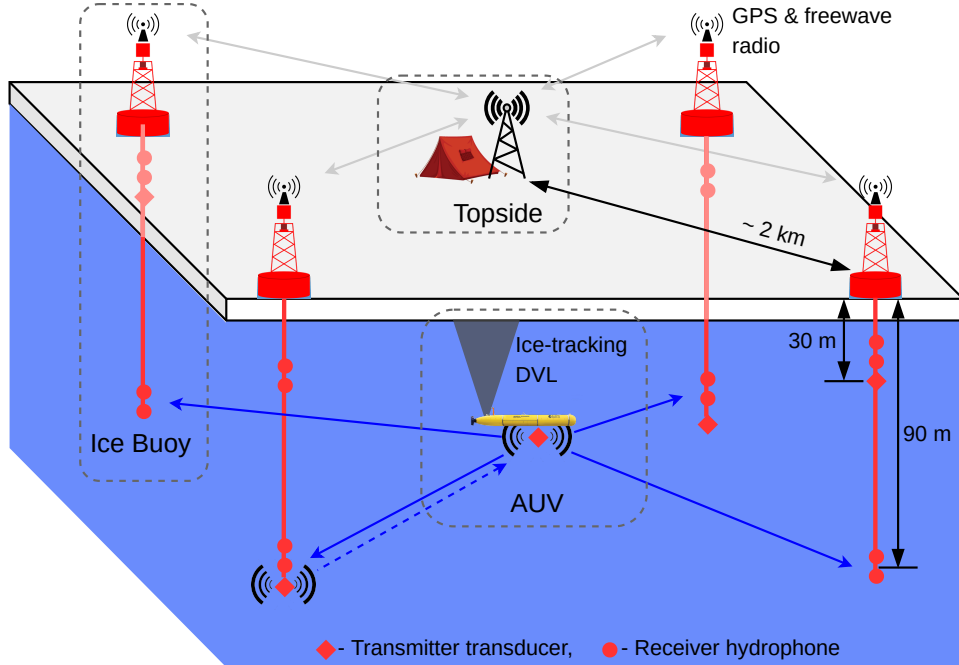


FIG. 1. A schematic overview of the Integrated Communication and Navigation Network (ICNN), which provides joint data-transfer and tracking between AUV and a human decision maker at Topside.

161 Micro-Modem ([Singh *et al.*, 2006](#)), with a four-element receiver array, a single transmitter,
 162 and one-tenth of a millisecond resolution. Acoustic messages were sent with a 10 kHz carrier
 163 frequency, 5 kHz bandwidth, and phase-shift keying (PSK) modulation on a time-division
 164 multiple access schedule with a thirty-second cycle, giving room for two-way communication
 165 throughout the mission volume. Thus the ICNN is dependent on the successful decoding of
 166 acoustic transmissions. The receive and transmit elements were split between shallow and
 167 deeper depths—30 and 90 m—to provide better coverage across the shadow zone. While
 168 each buoy only has one transmit depth, all buoys have both receive depths but the active
 169 receive layer is consistent across all buoys. The design of the ICNN enables a self-adapting

170 network to transmit and receive at the optimal depth to maintain contact with the AUV
 171 (Schneider *et al.*, 2021). The buoys do not encompass the full horizontal range of the vehicle
 172 but are positioned to minimize overlap in trilateration for spherical positioning (Deffenbaugh
 173 *et al.*, 1996a).

174 To balance competing uses of the acoustic channel, the network uses a single synchronized
 175 digital communication packet to provide both tracking and data to the operator.

176 1. The AUV, running an ice-tracking DVL and an onboard hydrodynamic model, broad-
 177 casts its perceived location on a scheduled, time-synchronized message via WHOI

178 Micro-Modem

179 2. Four ice buoys, each outfitted with a WHOI Micro-Modem, receive messages from the
 180 AUV and send that information over freewave radio to a Topside computer

181 3. The topside computer converts travel times into pseudorange estimates using a stochas-
 182 tic embedded prediction of the horizontal group velocity via BELLHOP ray tracing
 183 code (Porter, 2011) using a sound speed profile provided by an updatable Virtual
 184 Ocean (Bhatt *et al.*, 2022; Schneider and Schmidt, 2018)

185 4. The topside computer calculates a new position by trilaterating the range estimates

186 5. The position differential, not the absolute position, is broadcast to the vehicle to
 187 update its navigation solution and be robust to latency and intermittency

188 In the face of GNSS-denied navigation, this approach was anecdotally successful, as shown
 189 in Fig. 2. The AUV *Macrura* was deployed through a hydrohole from an ice camp but re-
 190 covered through an emergency hydrohole. A random disk error stalled *Macrura* underneath

the ice but did not prevent it from transmitting its location. Due to an incoming storm, a team drilled an exploratory hole at *Macrura*'s self-reported location, and were able to drill a separate hole 1 m away to tie the vehicle off to a physical marker on the ice. Three days later, *Macrura* was recovered—the ice camp had moved over 19 km. The AUV's relative position to camp had also changed, from roughly 45° at 1000 m to 90° at 1100 m. Drama aside, we view the emergency recovery as qualitative proof of the robustness of this navigation approach.

Nonetheless, this paper specifically addresses the third and fourth steps—the conversion of travel times into pseudoranges and its quantitative effect on trilateration. By focusing on pseudorange estimates between GPS-tracked beacons, and re-running the trilateration pipeline, the results are decoupled from all other mechanisms in the ICNN.

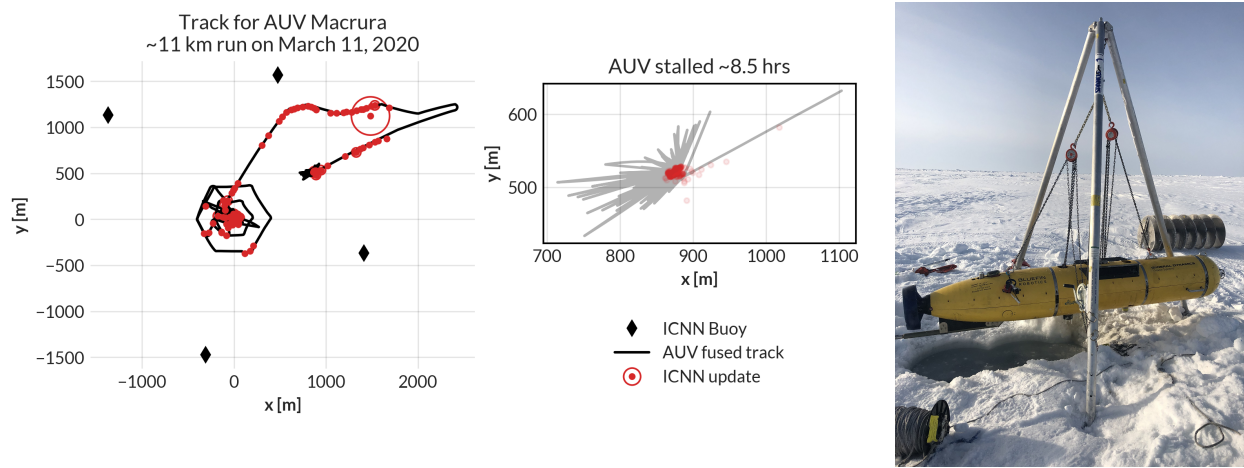


FIG. 2. The under-ice mission track for AUV *Macrura*, including the position updates as it stalled underneath the ice overnight. A marker was placed on the ice at the vehicle's estimated self-location. It was recovered after a three day storm within a meter of the marker.

201 **B. ICEX20 sound speed conditions**

202 An important component to our navigation solution is an accurate estimation of a repre-
 203 sentative SSP for the ocean volume. Previous field experience, during the Ice Exercise 2016
 204 (ICEX16), demonstrated the negative effects of the Beaufort Lens on tracking and commu-
 205 nication ([Schmidt and Schneider, 2016](#)). Fig. 3 shows historical, modeled, and *in situ* sound
 206 speed data for both ICEX16 and ICEX20. These three input streams were selected to mirror
 207 the information available on a submarine (personal conversation with LT B. Howard and LT
 208 CDR D. Goodwin). In the field, the SSP information was shared with the vehicle via basis
 209 representation compression on a lightweight digital acoustic message ([Bhatt et al., 2022](#)).
 210 All modeled data comes from HYCOM ([Chassagnet et al., 2007](#)), which does not seem to
 211 capture the forcing mechanisms that cause the Beaufort Lens. For ICEX16, the data-driven
 212 profile was sourced from nearby Ice Tethered Profilers (ITP) after the field experiment ([Kr-
 213 ishfield et al., 2008; Toole et al., 2011](#)) and exhibits a fairly deep lens; the historical profile is
 214 from the World Ocean Atlas. For ICEX20, the chosen weights (data-driven) profile derives
 215 from initial CTD casts taken on site, showing an intense warm water intrusion; the baseline
 216 (historical) profile, showing moderate ducted conditions, comes from the average of March
 217 2013 ITP data. This month best matched sea ice and sound speed conditions at the begin-
 218 ning of ICEX20 ([Bhatt et al., 2022](#)). It is important to note that all profiles that do show the
 219 Beaufort Lens do so with different local sound speed maxima at different depths, reflective
 220 of the wide range of lens properties observed for all ITP data in the region. The variability

²²¹ of the lens height and prominence is the main reason an updatable SSP was integrated into
²²² the ICNN solution.

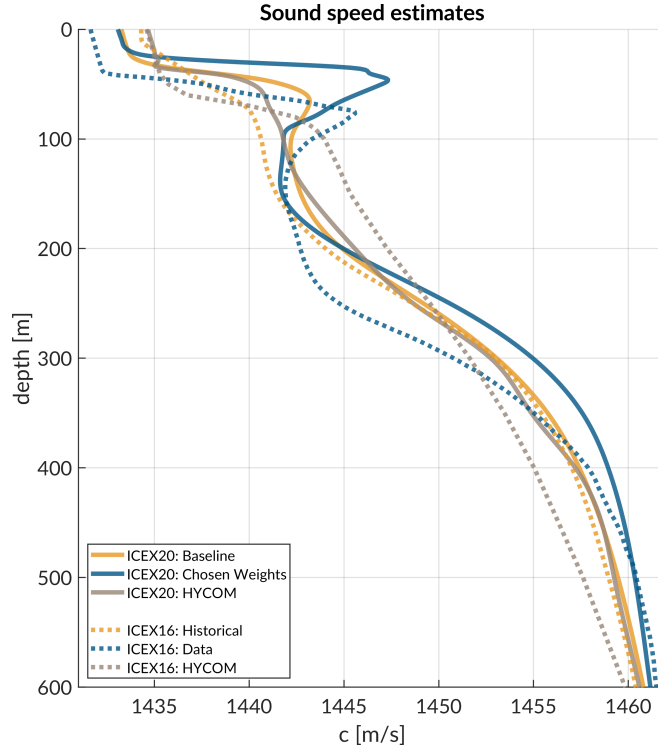


FIG. 3. Sound speed conditions for historical (baseline), data (chosen weights), and HYCOM model for both ICEX16 and ICEX20.

²²³ During ICEX20, the HYCOM profile was available but never deployed. For post-
²²⁴ processing comparison, we introduce both the HYCOM profile and an isovelocity case,
²²⁵ 1441.8 ± 3.7 m/s, as the mean and standard deviation of the observed sound speed profile
²²⁶ over the first 200 m. This is a contrived value taken in the style of [Graupe et al. \(2019\)](#)
²²⁷ for the sake of comparison; the default value in the LAMSS simulator, which was not envi-
²²⁸ ronmentally informed and used when no updates were available from the ICNN, was 1430
²²⁹ m/s.

230 **III. REAL-TIME PSEUDORANGE ANALYSIS**

231 Because the vehicle’s navigation solution during a mission can only be evaluated on the
232 basis of the error estimates sent, a sister experiment for validating the real-time ranging
233 approach was implemented. Ice buoy modems were run as “virtual vehicles” at a fixed
234 depth, receiving position updates from the other beacons as well as a camp site modem
235 lowered to 20 m. Fig. 4 shows successful events sorted by source depth. In this analysis, we
236 assume there is insignificant displacement between the GNSS puck surface expression and
237 subsurface modem; this is supported by unusually low observed ice drift rates, just 0.7 cm/s
238 on average throughout the mission.

239 **A. Minimal bounce (MB) criteria**

240 The fundamental challenge to implement GNSS-like navigation, especially in an acousti-
241 cally complex propagation environment, is characterizing a single sound speed to compensate
242 for the effects of ray refraction and reflection. The use of the acoustic modem network for
243 tracking relies on the accurate estimation of travel times between the submerged platform
244 and LBL beacons, supported by clock synchronization and a pre-determined scheduling of
245 acoustic events. For the Beaufort Lens in particular, the strong multipath effects make it
246 virtually impossible to deterministically predict the modem’s detected arrival time.

247 Instead, for each individual receiver i , an embedded stochastic tracking framework is used
248 to provide a running estimate of the effective sound speed $c_{i,j}$ for the conversion from travel
249 time to range from modem j , with the ultimate goal of matching the implied horizontal

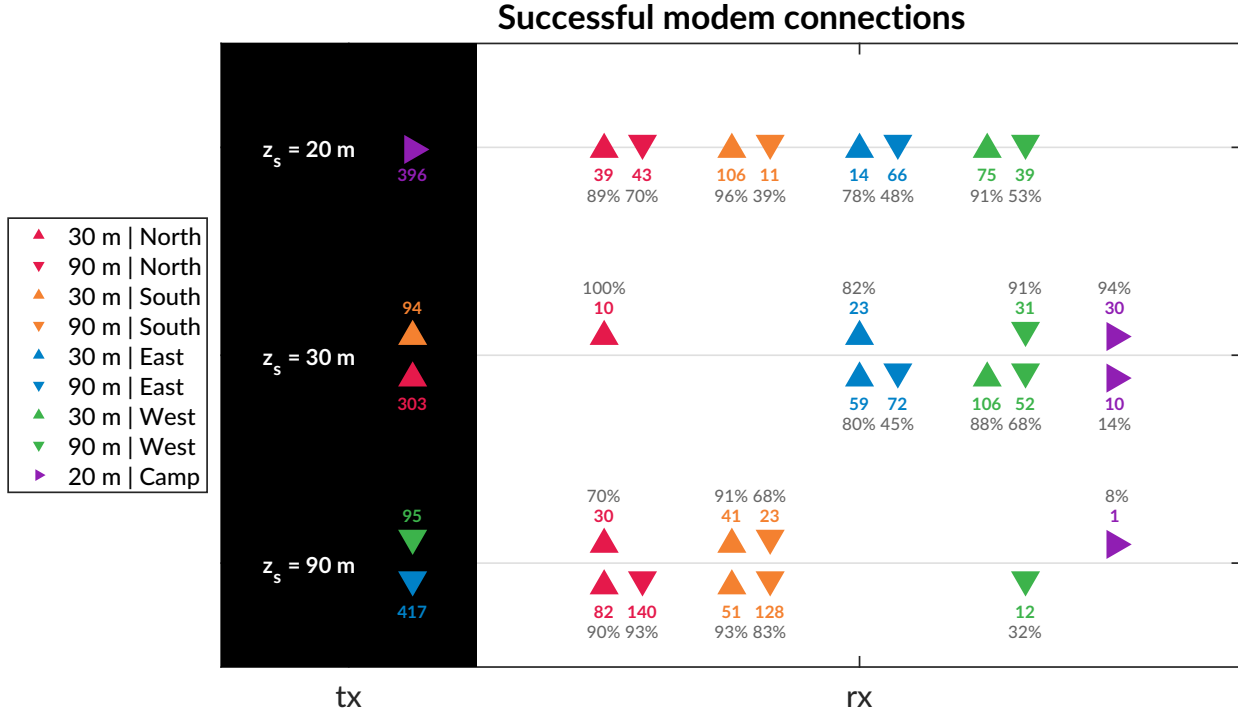


FIG. 4. An overview of the modem experiment by source and receiver depth and position. The black column on the left, *tx*, shows the source depth, z_s , with the total number of transmissions. The column on the right, *rx*, shows the receivers with the number of successful decodings and the percent success rate, defined as the ratio of decoded to detected. The orientation of the triangles—sideways, upwards, and downwards—corresponds to depths of 20, 30, and 90 m.

250 effective sound speed, i.e., the GPS-recorded distance between two nodes divided by the
 251 modem-recorded one way travel time between them.

252 In the ICEX20 configuration, the acoustic tracker is running on the topside computer,
 253 which controls the ICNN. Here we assume that the effective sound speeds $c_{i,j}$ are smoothly

254 varying over the course of a vehicle mission, i.e., with respect to range from signal origin at
 255 transmitter j , mission time, and the thirty-second frequency.

256 When the topside tracking framework receives a message, with a time delay, Δt , it will
 257 request a new estimate for $c_{i,j}$ along with its standard deviation. The effective sound speed
 258 is predicted using the vehicle's reported depth and the extrapolated navigation solution for
 259 range, \hat{r} , as inputs to the ray tracing program, which returns an impulse response estimate
 260 in the form of ray travel times dt_j and amplitudes a_j .

261 The initial call to BELLHOP is over a local grid centered at the range and depth posited
 262 by the onboard tracking solution. The grid, compared to a point solver, adds redundancy
 263 in resolving the actual multipath structure for a reliable acoustic path without overtaxing
 264 onboard computational time and memory. It is initialized as 11×11 points spanning 10
 265 m horizontally and 20 m vertically. The horizontal dimension reflects the accumulated
 266 vehicle position error given a thirty-second communication cycle; the vertical dimension
 267 reflects how, computationally, eigenrays of the same timefront seem to stack vertically in
 268 the water column. For each grid point, BELLHOP produces a number of arrivals resulting
 269 from multiple propagation paths. Using only the N_0 rays with neither surface nor bottom
 270 bounces, the tracking system will then estimate the current effective sound speed c from a
 271 power weighted average of the ray travel times,

$$c = \frac{\hat{r} \sum_{n=1}^{N_0} a_n^2}{\sum_{n=1}^{N_0} dt_n a_n^2}, \quad (1)$$

272 and the associated weighted standard deviation,

$$\sigma_c \simeq \sqrt{\frac{\sum_{n=1}^{N_0} (dt_n - \hat{r}/u)^2 a_n^2}{\sum_{n=1}^{N_0} a_n^2}} \frac{u^2}{\hat{r}} \quad (2)$$

²⁷³ If no direct paths exist, i.e. $N_0 = 0$, then the effective speed is computed using the same
²⁷⁴ algorithm for the ray arrivals with one bounce, and so on.

²⁷⁵ Finally, the pseudorange is calculated simply as

$$r_{i,j} = c_{i,j} \Delta t_{i,j} \quad (3)$$

²⁷⁶ Thus the minimal bounce (MB) criteria assumes the signal detected by the modem will
²⁷⁷ be dominated by a set of paths with the least number of boundary interactions. Impor-
²⁷⁸ tantly, this stochastic, ensemble method for group velocity calculation can run in real-time,
²⁷⁹ appearing to be orders of magnitude faster than other post-processing methods which seek
²⁸⁰ to determine the specific ray itself that best matches a prominent indicator from the arrival
²⁸¹ structure. The BELLHOP simulation that runs this calculation uses 3600 rays with launch
²⁸² angle fan of -60 to 60 degrees, a representative depth dependent sound speed profile, and a
²⁸³ range dependent bathymetry.

²⁸⁴ **B. Pseudorange error metrics**

²⁸⁵ The sister modem experiment generated 811 beacon to beacon communication events
²⁸⁶ with their own effective sound speed predictions from a real-time implementation of the
²⁸⁷ MB method. Given the complexity of the ICNN system, this experiment did not collect an
²⁸⁸ exhaustive set of data across all buoy, source depth, receive depth, and model sound speed
²⁸⁹ combinations. The algorithm generally overestimates pseudoranges because it resolves the
²⁹⁰ effective sound speed for the most direct path.

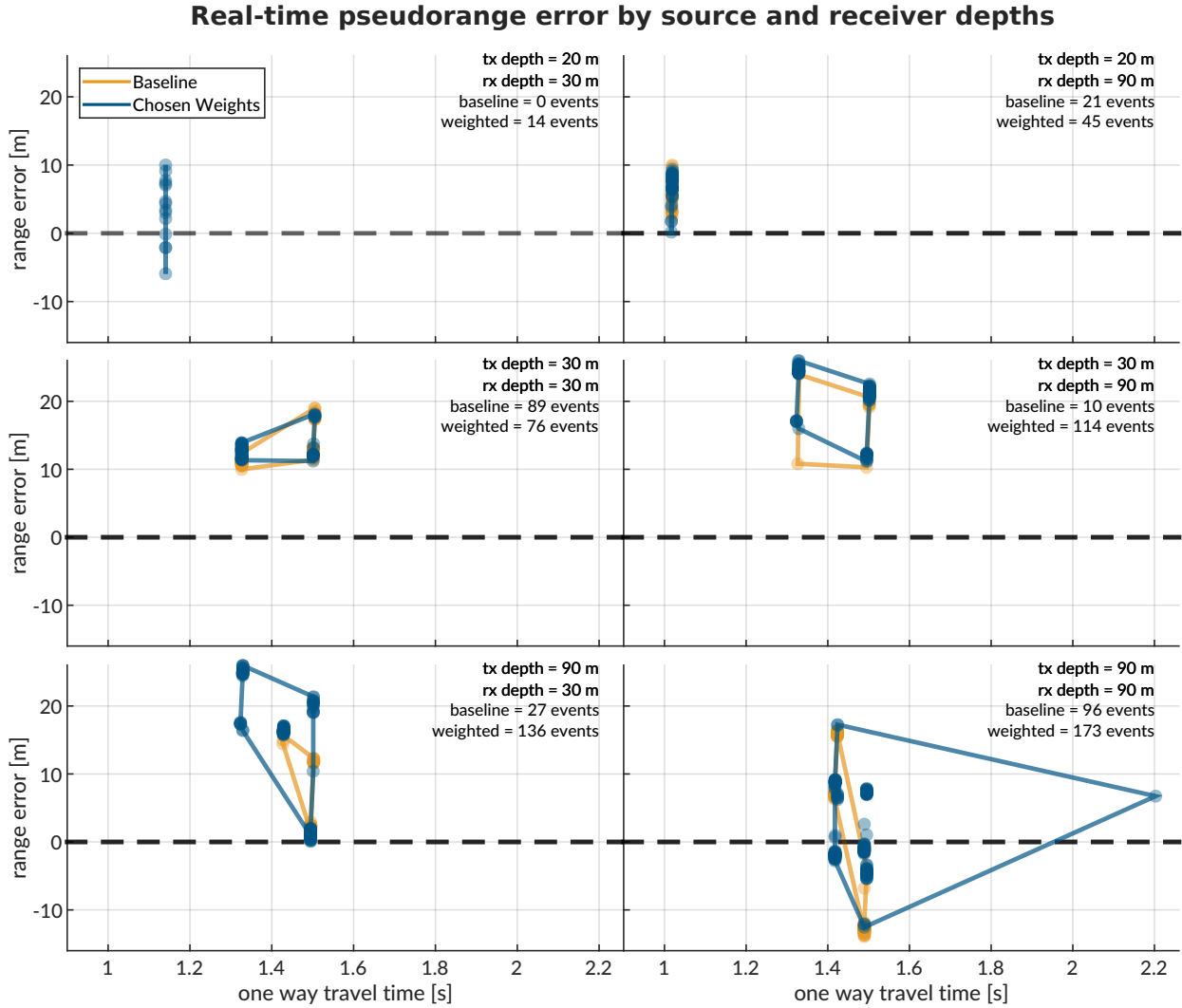


FIG. 5. The real-time range error by source (rows: 20, 30, and 90 m) and receiver (columns: 30 and 90 m) pairings for both sound speed estimates used during ICEX20. The amount of communication events is notated in the top right of each panel. The dashed line indicates no range error, and the boundary drawn indicates scope of the range error as a function of one way travel time.

Fig. 5 shows the range error boundary for both SSP inputs used in ICEX20. A promising sign that the MB method adapts sound speed somewhat intelligently is the lack of error growth as travel time increases. The baseline SSP ($n=243$ events) has an absolute pseudor-

294 range error of 11.38 ± 4.23 m; the weighted SSP ($n=568$), 11.36 ± 8.12 m. The discrepancy
 295 between these two is largely due to outlier events only contained in the weighted SSP set.
 296 Where there is overlap between sound speed conditions used for the real-time MB approach,
 297 the pseudorange error difference is no more than a few meters. The overarching results show
 298 that sound speed estimates derived from eigenrays for a local grid, as opposed to a singular
 299 point, are accurate enough to support vehicle navigation. While the MB looks for just the
 300 least complex multipath, the high density of launch angles almost always guarantees a direct
 301 path for the beacon-to-beacon configurations. Nonetheless, the consistent overestimation of
 302 pseudorange invites further analysis into acoustic arrival matching.

303 **C. Eigenray identification for beacon-to-beacon events**

304

305 Accounting for ice movement between beacons creates nominal ranges with small vari-
 306 ability. Figs. 6, 7, and 8 show eigenrays for three sound speed environments for source
 307 depths of 20, 30, and 90 m, respectively. Eigenrays were initially found using the built-in
 308 BELLHOP protocol with a launch angle fan of 2400 rays between -60 and 60 degrees. Sepa-
 309 rately, recorded travel times between beacons were clustered with 1 millisecond boundaries
 310 such that some source-receiver pairs had multiple, distinct travel times to approximate. The
 311 BELLHOP eigenray returns were then filtered such that one was selected per travel time
 312 cluster, in the hopes that the eigenray will converge to the receiver locations for the most
 313 realistic sound speed input. It should be noted that bottom bounces were recovered but

³¹⁴ filtered out. The three source depths create distinct ray geometries with respect to the three
³¹⁵ sound speed inputs.

³¹⁶ **1. Source depth of 20 m**

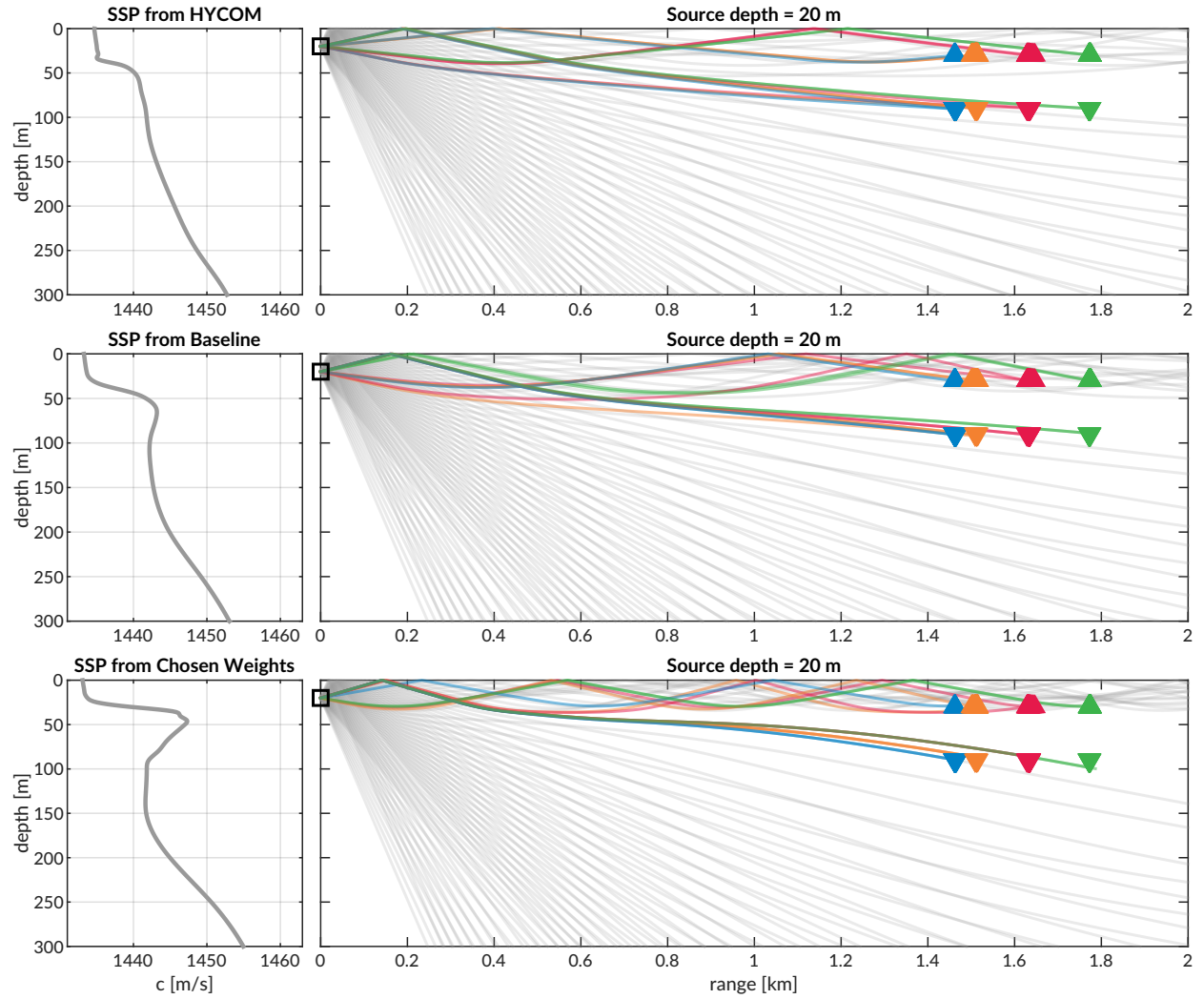


FIG. 6. Eigenrays for beacon-to-beacon events for each sound speed with a nominal source depth of 20 m over a total ray fan in gray. The beacons are highlighted in color/marker coding in Fig. 4.

317 For a source at 20 m in depth, shown in Fig. 6, reliable eigenrays are found for all sound
 318 speed inputs. Rays refract upwards and neatly intersect with the shallow and deep receiver
 319 locations between 1.5 and 1.8 km in range. However, the ray paths for the shallow receivers
 320 change both in the number of surface interactions and where the surface interactions occur
 321 with respect to range across the SSPs. As the Beaufort Lens strengthens, the chosen paths to
 322 the second farthest shallow buoy (North, in red) interact with the surface more and become
 323 distinct. The weighted SSP shows the most interesting effects for the deeper receivers. The
 324 ray paths all interact with the surface and the eigenrays for the Northern (red) and Western
 325 (green) buoys are in fact the same ray.

326 ***2. Source depth of 30 m***

327 The ray geometries from the 30 m source, shown in Fig. 6, show a similar degradation of
 328 eigenray identification with increased ducting. Receptions span 1.5 to 3.2 km. Once again,
 329 eigenrays for HYCOM and the baseline SSP are visually appropriate. Rays for the weighted
 330 SSP show how the surface channel intensifies ice interactions and how the shadow zone denies
 331 reliable acoustic paths. Pointedly, the increasing number of surface reflections to the farthest
 332 shallow buoy (North, in red) crystallize the MB criteria's tendency for overestimation. For
 333 the HYCOM, baseline, and weighted SSP inputs, the most appropriate eigenrays show 2, 3,
 334 and 4 surface interactions.

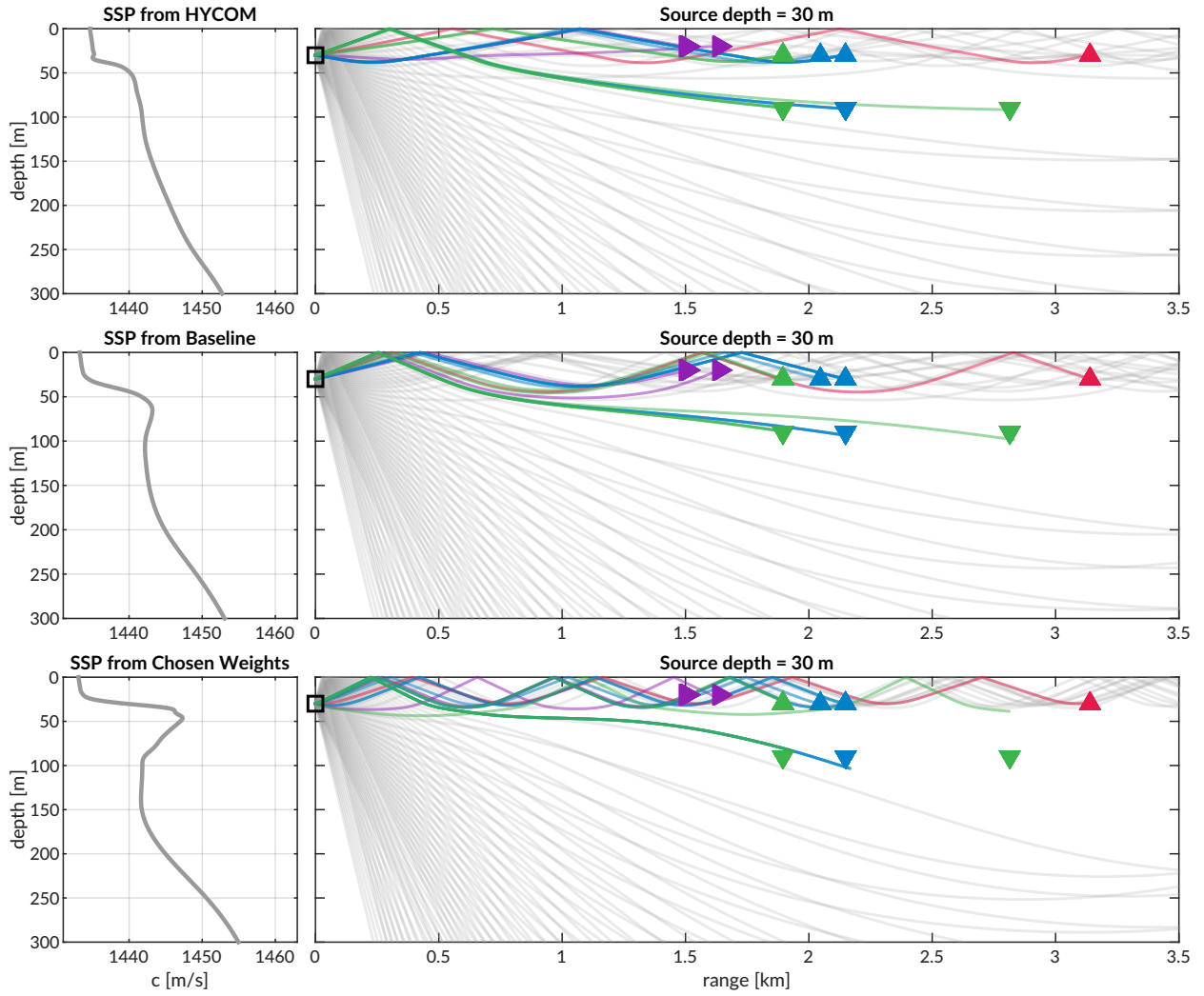


FIG. 7. Eigenrays for beacon-to-beacon events for each sound speed with a nominal source depth of 30 m over a total ray fan in gray. The beacons are highlighted in color/marker coding in Fig. 4.

335 ***3. Source depth of 90 m***

336 Lastly, Fig. 8 shows ray geometries from the 90 m source, elucidating a different extent
 337 of the shadow zone. While the receiver locations are similar to that of the 30 m source
 338 depth, the deeper source depth effectively negates the upper duct and places the upper (and
 339 some of the lower) receivers in unreliable acoustic paths. The HYCOM eigenrays still show

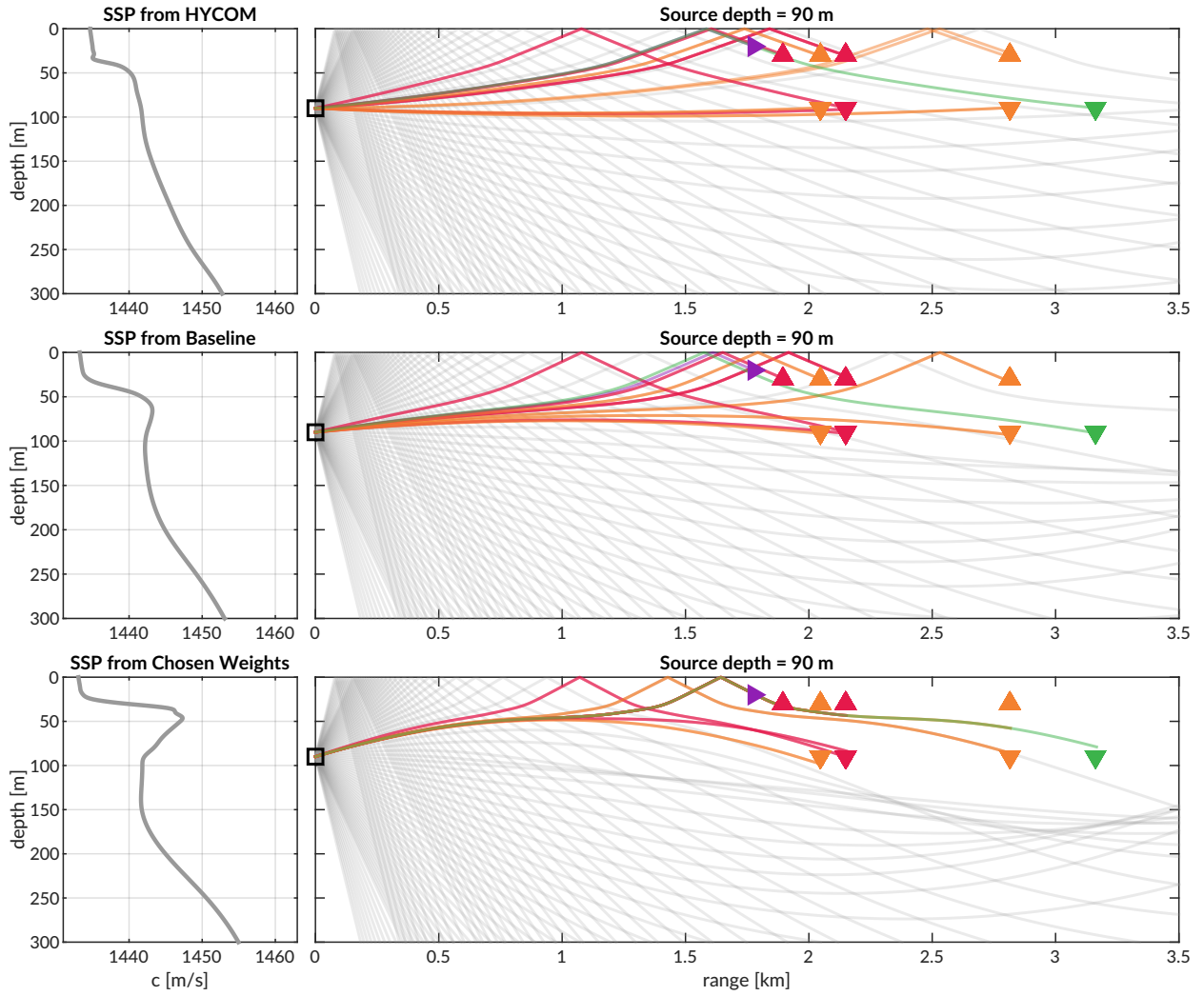


FIG. 8. Eigenrays for beacon-to-beacon events for each sound speed with a nominal source depth of 90 m over a total ray fan in gray. The beacons are highlighted in color/marker coding in Fig. 4.

340 the most reliable acoustic paths that deteriorate with increasing ducted conditions. The
 341 lack of direct paths from the observed SSP further points out the shortcomings of the MB
 342 approach.

343 The goal of the MB algorithm was to provide a reliable, physically intuitive interpretation
 344 of the acoustic propagation without taking on the additional burden of regularly identifying
 345 specific paths that may connect any given source-receiver pair in the network. While it

346 was unlikely to resolve multipath arrivals that triggered successful modem detection, an
347 isovelocity approach would have provided no adaptivity against source and receiver depth
348 differences. Its performance was adequate for vehicle navigation and would have likely
349 sufficed if it were not for the prominence of the duct observed relative that of other model
350 and data products.

³⁵¹ **IV. POST-PROCESSED PSEUDORANGE ANALYSIS**

³⁵² From all events recorded during the modem test experiment, there are 1242 successfully
³⁵³ decoded beacon-to-beacon events. Thus, a post-processing analysis that emulates the real-
³⁵⁴ time navigation engine was run to overcome the unequal distribution of communication
³⁵⁵ events with respect to depth, range, and sound speed status.

³⁵⁶ It is important to note that the value for the extrapolated range, \hat{r} , is only tracked by
³⁵⁷ topside for a modem claiming to be the vehicle; thus we replace \hat{r} with the GPS-tracked range
³⁵⁸ for all modem events. Because \hat{r} converges to the correct solution, a comparison of \hat{r} with
³⁵⁹ the GPS-tracked range shows a normal, zero-centered distribution within the bounds of GPS
³⁶⁰ drift. The analysis therefore seeds realistic but “omniscient” knowledge of the extrapolated
³⁶¹ range and emulates the post-processing pipeline to more thoroughly evaluate the acoustic
³⁶² pseudorange estimate for all modem events. Sound speed inputs are the isovelocity sound
³⁶³ speed in addition to the modeled, baseline, and weighted SSPs from Fig. 3. The analysis
³⁶⁴ replicates the MB criteria but also introduces a new filtering algorithm, the nearest bounce
³⁶⁵ (NB), based on insights gleaned from the eigenray analysis. Accordingly, the results in this
³⁶⁶ section evaluate the utility of the algorithms and sound speed sources, divorced from their
³⁶⁷ role in the ICNN while maintaining real-time relevance.

³⁶⁸ **A. Nearest bounce (NB) criteria**

³⁶⁹ The extent of ray bending and repeated reflections is extremely dependent on the degree of
³⁷⁰ the Beaufort Lens observed. Based on this insight, a new algorithm, the nearest bounce (NB)

³⁷¹ criteria, is a slight modification from the MB and includes multipath as a new dimension of
³⁷² information to exploit. This metric, while run in post-processing, adds a negligible amount
³⁷³ of computation for real-time efficacy.

³⁷⁴ Given a running estimate for the effective sound speed $c_{i,j}$ between nodes i and j , the
³⁷⁵ navigation system has an extrapolated value for range, \hat{r} , and a recorded travel time, $\Delta t_{i,j}$.
³⁷⁶ Instead of using only the N_0 rays with neither surface nor bottom bounces to estimate
³⁷⁷ conversion speed, and subsequently moving to incremental number of bounces only when no
³⁷⁸ valid direct path solutions exist, we solve for the power weighted average of the ray travel
³⁷⁹ time for the N_k rays with k bounces,

$$t_k = \frac{\sum_{n=1}^{N_k} dt_n a_n^2}{\sum_{n=1}^{N_k} a_n^2}, \quad (4)$$

³⁸⁰ find the nearest matching power weighted average to recorded travel time,

$$t_{i,j,k} = \min_{k=0,1,2,\dots} |t_k - \Delta t_{i,j}| \quad (5)$$

³⁸¹ predict an effective sound speed,

$$c_{i,j} = \frac{\hat{r}}{t_{i,j,k}} \quad (6)$$

³⁸² and estimate the range as was done previously.

$$r_{i,j} = c_{i,j} \Delta t_{i,j} \quad (7)$$

³⁸³ Whereas the MB outputs a scalar, this method first outputs a vector of effective sound
³⁸⁴ speeds based on the number of reflections. Then a single value is selected in a nearest-
³⁸⁵ neighbor fashion that best matches the recorded travel time, as the detected arrival is not
³⁸⁶ always the first arrival or the direct path and could even be masked by noise or blocked

387 temporarily (Deffenbaugh *et al.*, 1996b). We manually cap the number of bounces at four
388 because of the smaller operational scale and the attenuation accrued with many surface
389 interactions. Bottom bounces are not encoded separately because ray's tendency to
390 refract upward, not due to information limitations.

391 **B. Effective sound speed predictions**

392 The minimal and nearest bounce algorithms are applied with the three sound speed inputs
393 shown in Figs. 6, 7, 8. The resulting predicted effective sound speeds are shown in Fig. 9
394 for all source depths versus one way travel time.

395 The goal of the effective sound speed prediction is to converge towards the implied sound
396 speed, i.e. the GNSS-derived range divided by the recorded travel time. As the environ-
397 mental and ray filtering method become better representations of the real ocean, the lower
398 the expected mismatch is between the implied and estimated effective sound speeds.

399 The various sound speed inputs—isovelocity aside—not only modify the predicted effec-
400 tive sound speed, as seen by the colored vertical offsets, but often classify a distinct number
401 of bounces. HYCOM sees the most direct and one bounce multipath structures, lending a
402 bias for faster speeds; the weighted SSP sees the most double and triple bounces, favoring
403 slower speeds; the baseline sound speed exists in between. Very rarely is the multipath
404 structure classified as a direct path, i.e., where the NB defaults to the MB prediction. In
405 fact, the higher the multipath classification, the more accurate the sound speed prediction
406 is, likely driven by a tighter or even sparser bundle of rays. Discontinuities in multipath
407 classification provide initial evidence for its importance to a smoothly varying group velocity,

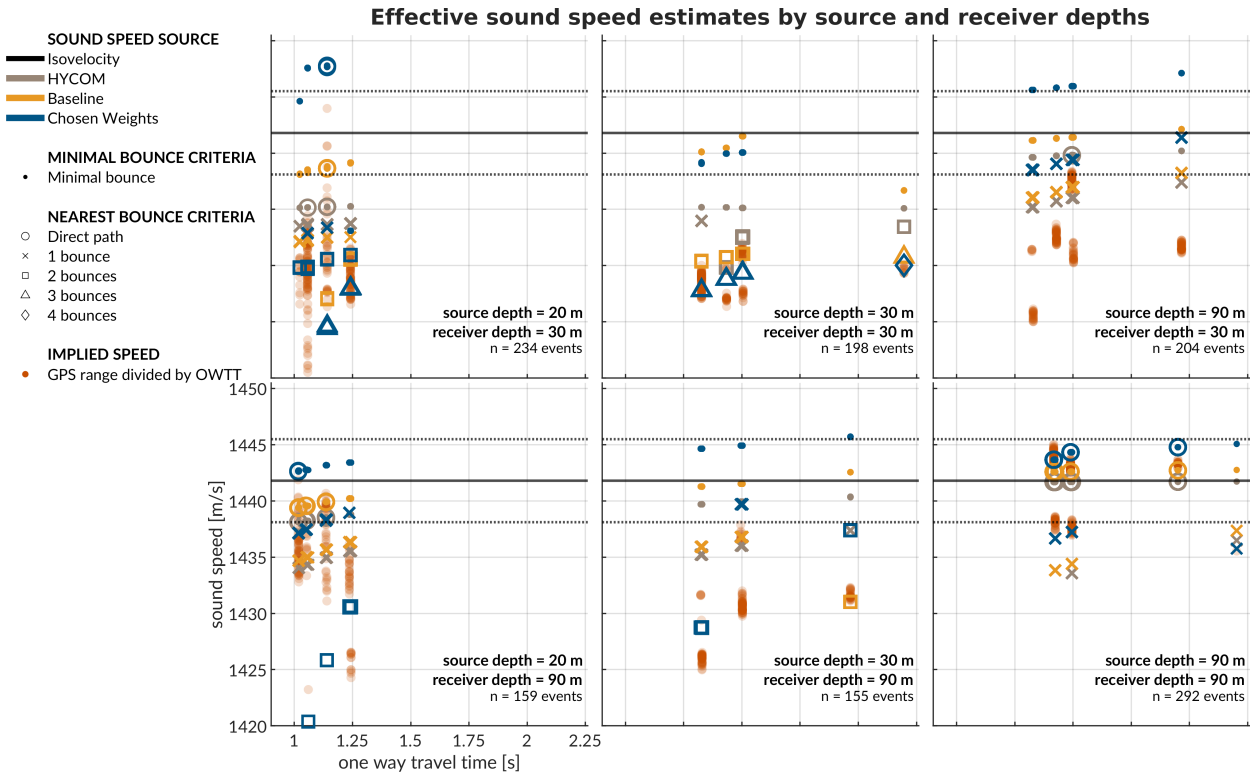


FIG. 9. A post-processing comparison of effective sound speed predictions for all beacon-to-beacon events. The rows share receiver depth; the columns share source depth. The recorded travel time is on the x-axis and the predicted effective sound speed is on the y-axis. The sound speed source is indicated by color. The isovelocity is shown as the mean \pm the standard deviation. The minimal and nearest bounce criterion are distinguished by different marker shapes, compared to the separately colored red dots showing the implied calculation.

as shown in the cluster of 30 to 30 m transmissions in Fig. 9, where HYCOM jumps from one to two classified bounces amidst the baseline SSP and weighted SSP smoothly increasing while consistently seeing two and three classified bounces, respectively. Of course, the prediction deteriorates with cross-layer transmissions across the duct, but not to the same degree at which eigenrays could not be found for the weighted SSP in section III C. The

⁴¹³ evidence suggests that the grid based method provides a useful amount of redundancy to
⁴¹⁴ resolve similar enough eigenrays.

⁴¹⁵ It is useful to think about in what case the isovelocity—or any isovelocity framing—would
⁴¹⁶ have been appropriate. The transmissions from shallow to shallow receiver may have
⁴¹⁷ matched the default configuration of 1430 m/s. The isovelocity contrived for this paper,
⁴¹⁸ 1441.8 m/s, best matches the transmissions from 90 to 90 m. The one from [Graupe *et al.*](#)
⁴¹⁹ ([2019](#)), 1450 m/s, would have had a systemic overestimation. In addition, over the course
⁴²⁰ of the four day experiment, the local maxima of the Beaufort Lens changed from roughly
⁴²¹ 1447 m/s at 40 m to 1442 m/s at 60 m. Given that implied sound speeds just for beacon-
⁴²² to-beacon events span 1420 to 1445 m/s, it is safe to say that a nominal sound speed would
⁴²³ sacrifice pseudorange accuracy somewhere, and that an adaptive approach is necessary even
⁴²⁴ for short and/or small scale operations in the Beaufort Lens.

⁴²⁵ C. Pseudorange error metrics

⁴²⁶ Pseudorange estimation plays an important role in trilateration. Fig. [10](#) shows the
⁴²⁷ directional pseudorange error “footprints” for the four sound speed inputs with the NB
⁴²⁸ approach, separated by source and receiver depth configurations.

⁴²⁹ The weighted SSP range error generally has the smallest and most zero-centered footprint.
⁴³⁰ The one case it does not is for the source-receiver pairings between 30 and 90 m in depth. The
⁴³¹ increased error for these is most likely driven by the computational artifacts encountered
⁴³² when propagating through the steep sound speed gradients of the lens and through the

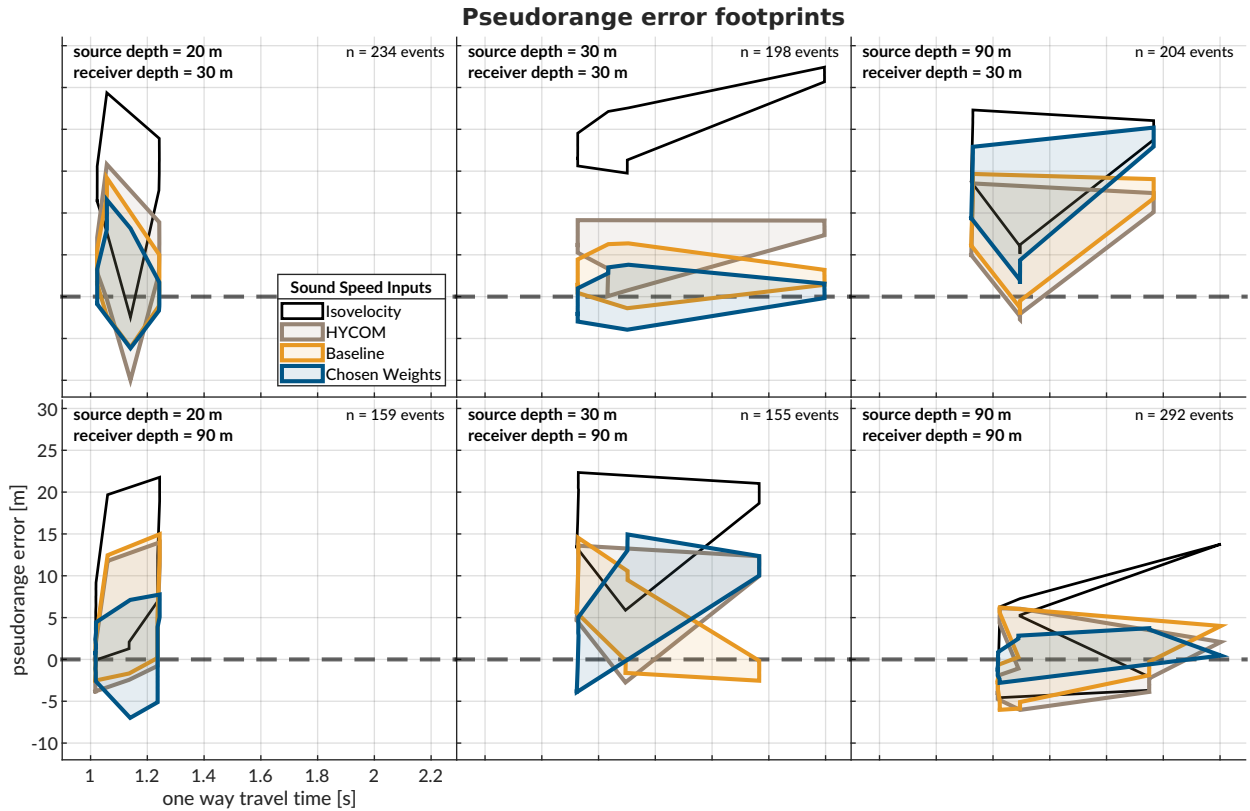


FIG. 10. The post-processed pseudorange error; the rows share receiver depth; the columns share source depth. The dashed gray line shows no error. The shaded region connects the range performance across all events.

⁴³³ shadow zone. All other source depth pairings are significantly improved using the chosen
⁴³⁴ weights compared to HYCOM or the baseline.

⁴³⁵ When using a linear scaling to convert travel time into range, any offset between the
⁴³⁶ assumed sound speed and the horizontal group velocity produces unconstrained error with
⁴³⁷ increasing receiver distance, whereas an adaptive estimate would exhibit no such trend. This
⁴³⁸ is easily observed in the same-layer links, i.e., 30 to 30 m and 90 to 90 m. In cross-layer
⁴³⁹ links, the isovelocity does not perform better but tends to exaggerate or flip the footprint
⁴⁴⁰ created adaptively.

441 The improvement from MB to NB is most evident for the data-driven sound speed;
442 while the HYCOM SSP improves from a median absolute range error of 6.41 to 4.61 m,
443 the baseline SSP improves from 10.30 to 2.27 m, and the weighted SSP improves from
444 13.28 to 2.12 m. In comparison, the isovelocit y has a median error of 13.09 m. The order
445 of magnitude improvement in the ducted SSPs demonstrate the effectiveness of the NB
446 algorithm exploiting the observed multipath conditions.

447 There is one example that helpfully illustrates the improvement brought upon by bounce
448 classification. For transmissions between North and South at 30 m, the OWTT spread is
449 2.1958 to 2.1963 s; the GNSS-tracked distance is 3138.54 to 3140.87 m; and the implied
450 effective sound speed is 1429.3 to 1430.1 m/s. For these transmissions, the weighted SSP
451 and the MB approach produce a pseudorange error of -1491 m, as the effective sound speed
452 predicted by the minimum bounce criteria is dominated by bottom bounce arrivals with
453 much greater travel times. The NB approach categorizes this same record as a quadruple
454 surface bounce, reducing the pseudorange error to less than a meter. Comparatively, the NB
455 approach for HYCOM and the baseline SSP produce pseudorange errors of 8.30 and 2.39
456 m, respectively. There is strong evidence to suggest that the sound speed and multipath
457 fidelity codependently improve localization accuracy.

⁴⁵⁸ **V. TRILATERATION FOR ICEX20 FIELD DATA**

⁴⁵⁹ To overcome potentially intermittent acoustic communication, the operational paradigm
⁴⁶⁰ of the ICNN computes corrections relative to the trilaterated position estimates transmitted
⁴⁶¹ by the vehicle, rather than transmitting the updated positions themselves. The reliability
⁴⁶² of the correction is directly linked to how accurately the travel time measurements are
⁴⁶³ converted to pseudoranges. This section aims to resolve that tension by reevaluating the
⁴⁶⁴ trilateration results with respect to the MB and NB algorithms. The MB/NB effective
⁴⁶⁵ speed predictions were tracked independently for each source-receiver pair; although the
⁴⁶⁶ sound speed was expected to be locally smooth near a given receiver, no such assumption
⁴⁶⁷ was enforced between distinct acoustic links.

⁴⁶⁸ **A. Re-positioning beacon to beacon events**

⁴⁶⁹ When the beacons ran as virtual vehicles, the ICNN did not have access to that buoy's
⁴⁷⁰ GPS data stream except for what was sent via digital acoustic message. The static nature
⁴⁷¹ of the experiment means that the initial estimate transmitted to the ICNN was in fact a
⁴⁷² ground truth position. Therefore, a distribution of corrections from the ICNN, as shown in
⁴⁷³ Fig. 11, reflects positioning accuracy. The NB clearly outperforms the MB, with almost 80%
⁴⁷⁴ of the corrections below 6 meters and the median within the deployed GNSS puck precision
⁴⁷⁵ of 3 meters. By contrast, the MB shows roughly 20% within the GNSS puck precision,
⁴⁷⁶ and separate peaks from 9–12 meters and 21–27 meters. This trimodal nature reflects the
⁴⁷⁷ distribution of reflections on the ice surface.

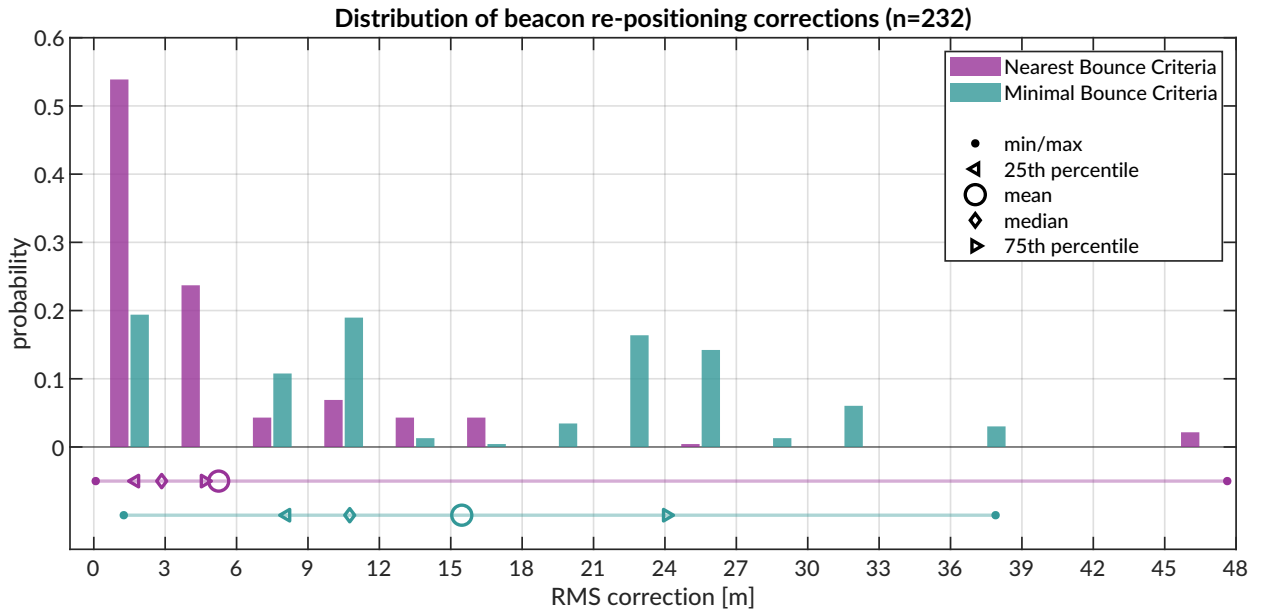


FIG. 11. Trilateration events; however, 264 entries are 2-beacon solutions, 22 are 3-beacon, and 2 are 4-beacon. When limited to only two ranging circles, the trilateration chooses the closer of the two intersection points. The x-axis is cut off at the upper limit for the NB algorithm.

478 In several events, the MB is unable to accurately estimate the effective sound speed for
 479 one of the acoustic links, leading to a large positioning error. The NB, however, better
 480 resolves an approximation of the acoustic path. For example, in some trilateration solutions
 481 for the Eastern buoy, the MB shows a correction of more than a kilometer; the NB is two
 482 orders of magnitudes less.

483 **B. Re-navigating AUV *Macrura***

484 Up to this point, pseudorange estimation and localization have been evaluated on GPS-
 485 linked beacon-to-beacon connections to validate the NB algorithm. This analysis ports the
 486 MB and NB algorithms to re-navigate the AUV *Macrura*.

487 In comparison to the modem experiment, the AUV data clearly exhibit instances where
488 a receiver detects the same transmission more than once. This is not surprising considering
489 the complex multipath provided by the Beaufort Lens. The 11 hour vehicle mission con-
490 tains 3,260 transmissions, 12,938 total detections, and 4,704 successful receptions. Allowing
491 receptions with PSK errors would almost double the number of recorded multipath arrivals
492 exploited for positioning, if a real-time solution could correctly parse paths from different
493 arrivals in the same thirty-second cycle. Thus it remains a future endeavor to explore how
494 failure mode information from acoustic modems could be used to identify unsuccessful but
495 otherwise trustworthy arrivals to augment trilateration samples.

496 The following performance analysis is constrained to what the vehicle acted on in real-
497 time. AUV *Macrura* and the ICNN ran an adaptive depth behavior to maintain acoustic
498 communication on the insight that cross-layer links were more likely to fail than same-layer
499 ones. Accordingly, the vehicle dove deeper than 50 meters about 20% of the time it was
500 underway.

501 In contrast to the modem tests, where position correction illustrated re-positioning ac-
502 curacy, the re-navigation corrections are less valuable in the absence of GNSS ground truth.
503 The correction magnitude necessarily depends on the vehicle's internal navigation estimate,
504 which is prone to larger errors from sensor drifts, ocean currents, and other error not cap-
505 tured in the hydrodynamic model. Thus, larger corrections are not necessarily indicative of
506 worse performance. Navigation accuracy is better described by trilateration error, the RMS
507 of the remaining pseudorange errors from each acoustic link.

508 Fig. 12 shows the correction magnitudes and trilateration errors for events with three or
 509 more receptions during AUV operations. Whereas the MB has a fairly bimodal nature, with
 510 peaks centered around 10–15 and 35–40 m, the NB favors smaller corrections, from 5–20 m,
 511 and has a long tail. The distribution of corrections are much larger than the distribution
 512 of RMS error. It is apparent that, while both methods are quite successful, there is strong
 513 evidence that the NB achieves single meter accuracy.

514 C. Investigating potential GNSS noise

515

516 The fact that the bulk of the best performing re-navigation error exists within the preci-
 517 sion of the GNSS unit deployed invites a further look into GNSS noise. In the Arctic, GNSS
 518 performance worsens due to poor constellation coverage, larger ionospheric effects, and mul-
 519 tipath interference (Gwal and Jain, 2011; Jung *et al.*, 2018; National Research Council, 2011;
 520 Reid *et al.*, 2016; Swarlund *et al.*, 2016; Themens *et al.*, 2015). Radio infrastructure that
 521 provides position corrections and references does not regularly extend to polar regions. The
 522 effect is minor for surface platform navigation —roughly 15 m of horizontal precision has
 523 been displayed at the North Pole—but is significant enough to register against the modem’s
 524 detected travel times. Fig. 13 zooms in on the GNSS and OWTT noise relative to the ice
 525 movement for two pairs of modem buoy connections. The two panels indicate the GPS noise
 526 as $\delta R = \sqrt{\delta x^2 + \delta y^2}$ and temporal drift, δt , relative to the median OWTT recorded between
 527 the two modems. The dashed line is scaled by a group velocity of 1440 m/s, such that if

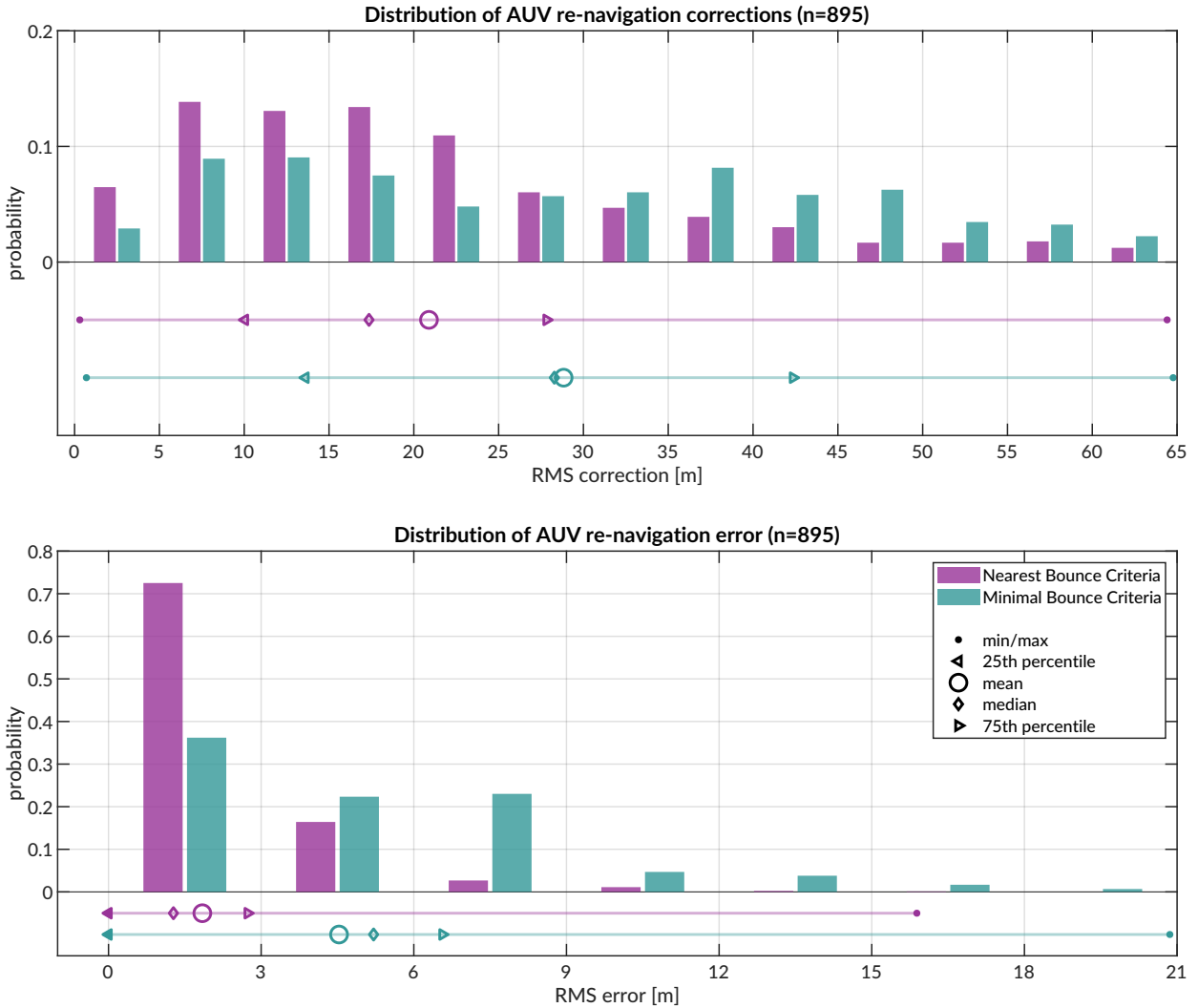


FIG. 12. Distribution of vehicle re-navigation corrections (top) and error (bottom) computed in post-processing for the Minimal and Nearest Bounce Criterion.

528 there were ideal sensor measurements with no drift, all events should exist on or near the
 529 line.

530 The left panel shows the connections between the North and East buoys. The clusters
 531 scaling along the 1440 m/s guideline suggest relative ice movement picked up by both GNSS
 532 and OWTT. But the vertical distribution across many arrival time bands is indicative of

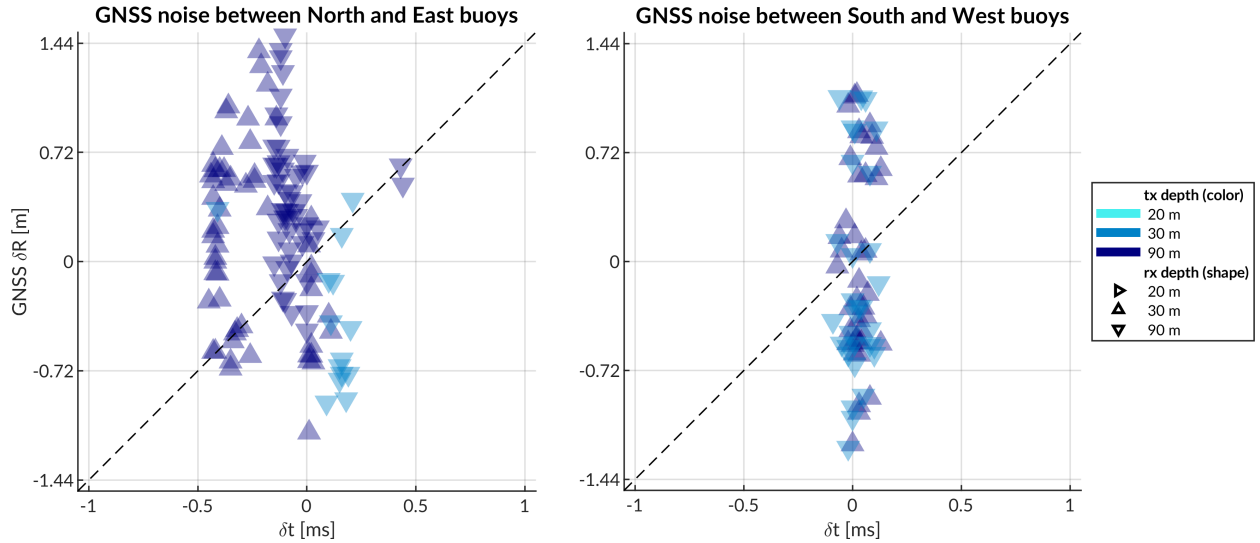


FIG. 13. A comparison of GPS noise (y-axis) versus OWTT drift (x-axis) for corners of the ICNN network with different source depths.

the GNSS fluctuations in precision, or noise. Some minor offsets between these vertical bands relate to different operational configurations of source and receiver depth. The idea of GNSS noise relative to OWTT is further indicated by events between two other buoys, South and West. The relatively thin time window suggests these buoys are moving in a more rigid ice floe and that there is minimal impact by source and receiver depth on the spread of OWTT. Yet, the vertical distribution, spanning almost 4 meters, cannot be explained by time differentials due to acoustic scattering, multipath, and/or environmental microstructure. This conclusion corroborates the vertical spread of implied effective speeds in Fig. 9.

⁵⁴² **VI. DISCUSSION**

⁵⁴³ Underwater navigation research is broadly motivated by acquiring GNSS-like navi-
⁵⁴⁴ gation in GNSS-denied conditions. Accurate range estimation is essential to mitigating error.
⁵⁴⁵ Current approaches for underwater acoustic navigation simplify the non-linear relationship
⁵⁴⁶ between a SSP and timefronts with a deterministic sound speed. Thus, the conversion of
⁵⁴⁷ travel time into distance can be pre-conditioned for error and error growth over the course
⁵⁴⁸ of a vehicle mission. This work introduces a lightweight stochastic prediction of an effec-
⁵⁴⁹ tive speed along the acoustic path between source and receiver, retooling arrival methods
⁵⁵⁰ generally deemed too complex or labor intensive for real-time. We assume that the effec-
⁵⁵¹ tive sound speed would be a locally smoothly varying function with respect to operational
⁵⁵² conditions—horizontal and vertical differences and rate of difference between source and re-
⁵⁵³ ceiver. The field-tested approach, the minimal bounce criteria, facilitated a successful AUV
⁵⁵⁴ recovery in a total ice-covered, double ducted environment. The accuracy of the MB was
⁵⁵⁵ validated against GPS-linked beacon-to-beacon communications. Given a consistent bias
⁵⁵⁶ towards overestimation, an improved algorithm, the nearest bounce criteria, was developed
⁵⁵⁷ on the insight that multipath structure may play an outsized role in maintaining a smoothly
⁵⁵⁸ varying effective sound speed. The NB was developed with field data and reevaluated on
⁵⁵⁹ vehicle data, achieving a position accuracy and precision that compares with that of the
⁵⁶⁰ deployed GNSS puck.

⁵⁶¹ A key insight for both approaches was seeking an eigenray ensemble around an estimated
⁵⁶² location instead of seeking to unambiguously match arrivals. The ensemble diversified the

563 simulated multipath possibilities to better capture the actual multipath recorded. In this
564 way, the solution exploits multipath, generally viewed as a source of uncertainty, as a new
565 dimension of information to improve localization accuracy. Based on the navigation and re-
566 navigation results of our AUV deployment in the ice-covered Beaufort Sea, we conclude that
567 embedding a model-aided prediction of the effective sound speed has an outsized benefit
568 to minimizing trilateration error, and that our approach sufficiently resolves the acoustic
569 timefronts for an unpredictable, complex propagation environment like the double ducted
570 Beaufort Lens.

571 There are many avenues through which this approach can be further refined and tested for
572 field operations. Amongst them is defining the uncertainty grid for BELLHOP via stochastic
573 or data-driven measures such as the distance traveled by the AUV between ICNN updates
574 or the magnitude of the position corrections by the ICNN. Another is to entirely remove the
575 seeded range and instead rely on the submerged asset's depth and recorded OWTT to find
576 high probability fields in range.

577 The relatively simple nature of this approach suggests it is transferable to other envi-
578 ronments, spatio-temporal scales, and platforms. While it is likely a particular quirk of
579 the Beaufort Lens that filtering for reflection alone can produce a horizontal effective speed
580 that compensates for ray refraction and reflection, the algorithm can be reconditioned to
581 filter against other metrics, like number of turning points, to create a more diverse and in-
582 formed set of multipath timefronts. Though the majority of re-navigation results are within
583 single-meter accuracy, future work can examine how constellations of more LBL beacons
584 can extend the operational domain without adding an undesirable amount of error. One

585 possibility is that, during a mission, ICNN-like LBL implementations use a comparison of
586 the GNSS self-position and acoustic positioning to invert for the ocean volume, linking how
587 vertical and horizontal sound speed structure impact transmission integrity. A fast tomo-
588 graphic estimate (Deffenbaugh, 1997; Elisseeff *et al.*, 2002), along with its uncertainty, could
589 be continuously communicated to assets underway to maintain contact or enable adaptive
590 sampling. In this sense navigation and tomography converge on the same set of compo-
591 nent technologies—position estimation, sound speed parameterization estimation, ray path
592 identification, and vehicle path optimization.

593 Spatio-temporal variability is a serious challenge for accurate real-time ranging. On
594 one hand, the effectiveness of eigenray filtering algorithm is likely only challenged by the
595 valid operational scales of a range independent propagation environment. Longer range
596 experiments may provide more time for eigenray filtering. A bootstrapping approach that
597 filters eigenrays for several randomly generated internal wave spectrums may compensate
598 for otherwise unknowable spatio-temporal variability. The model-aided component to the
599 eigenray filtering is compatible with vertical slices from any physically driven ocean model.
600 But in the long run, more accurate and higher resolution global circulation models are
601 needed to properly resolve features that alter ducted propagation at the scales discernible
602 to an acoustic modem. Through-the-sensor methods can resolve local features but would
603 require a degree of information sharing not readily supported on the acoustic channel for
604 large scale variability. But addressing the spatial and temporal scales of what can be solved
605 deterministically and what must be solved stochastically imposes a resolution constraint
606 that is at odds with computational overhead for real-time operations. Resolving features

607 inaccurately, or with a false sense of confidence, could be more harmful than contextualizing
608 the limitations of a range independent propagation over realistic bathymetry. Given that
609 AUV operations are often on smaller spatial and temporal scales, the added benefit of an
610 ocean model is quite small, and for features like the Beaufort Lens, not well resolved.

611 The methods involved in this paper include open source software projects ([Benjamin *et al.*, 2010](#),
612 [Schneider *et al.*, 2015](#); [Schneider and Schmidt, 2010](#)) that are platform agnostic. Large
613 AUVs, often large enough to support long duration and/or deep sea missions, would benefit
614 from including diurnal or tidal effects for ranging. Gliders, though generally low power and
615 memory, have been equipped with acoustic modems. Their inability to maintain position
616 within a region of reliable acoustic path makes the impact of an environmentally adaptive
617 pseudorange estimation disproportionately positive. The exact adjustments to the ensemble
618 eigenray filtering are predicated on the expected sound speed conditions and acoustic arrival
619 structure; the problem is ripe for other simulation testbeds or machine learning methods.
620 The continued development of embedded acoustic processing on heterogenous platforms is
621 fundamental to support a universal underwater navigation scheme comparable to GNSS.

622 **ACKNOWLEDGMENTS**

623 We acknowledge the significant operational effort spearheaded by the LAMSS ICEX20
 624 team and all our collaborators. Bhatt was funded by a National Defense, Science, and
 625 Engineering Graduate Fellowship. This work was supported by the Office of Naval Research
 626 322-OA under ICEX20 (N00014-17-1-2474) and Task Force Ocean (N00014-19-1-2716).

627 ¹Also at MIT-WHOI Joint Program in Oceanography/Applied Ocean Science & Engineering, Cambridge,

628 MA

629

630 Ballard, M. S., Badiey, M., Sagers, J. D., Colosi, J. A., Turgut, A., Pecknold, S., Lin,
 631 Y.-T., Proshutinsky, A., Krishfield, R., Worcester, P. F., and Dzieciuch, M. A. (**2020**).
 632 “Temporal and spatial dependence of a yearlong record of sound propagation from the
 633 Canada Basin to the Chukchi Shelf,” The Journal of the Acoustical Society of America
 634 **148**(3), 1663–1680, doi: [10.1121/10.0001970](https://doi.org/10.1121/10.0001970).
 635 Barker, L. D., Jakuba, M. V., Bowen, A. D., German, C. R., Maksym, T., Mayer, L.,
 636 Boetius, A., Dutrieux, P., and Whitcomb, L. L. (**2020**). “Scientific challenges and present
 637 capabilities in underwater robotic vehicle design and navigation for oceanographic explo-
 638 ration under-ice,” Remote Sensing **12**(16), 1–31, doi: [10.3390/RS12162588](https://doi.org/10.3390/RS12162588).
 639 Bellingham, J. G., Leonard, J. J., Vaganay, J., Goudey, C. A., Atwood, D. K., Consi,
 640 T. R., Bales, J. W., Schmidt, H., and Chrysostomidis, C. (**1995**). “AUV operations in
 641 the Arctic,” in *Sea Ice Mechanics and Arctic Modeling Workshop*.

- 642 Benjamin, M. R., Schmidt, H., Newman, P. M., and Leonard, J. J. (2010). “Nested au-
 643 tonomy for unmanned marine vehicles with MOOS-IvP,” Journal of Field Robotics **27**(6),
 644 834–875, doi: [10.1002/rob.20370](https://doi.org/10.1002/rob.20370).
- 645 Bhatt, E. C. (2021). “A Virtual Ocean framework for environmentally adaptive, embed-
 646 ded acoustic navigation on autonomous underwater vehicles,” Ph.D. thesis, Woods Hole
 647 Oceanographic Institution, doi: [10.1575/1912/27309](https://doi.org/10.1575/1912/27309).
- 648 Bhatt, E. C., Howard, B., and Schmidt, H. (2022). “An Embedded Tactical Decision Aid
 649 Framework for Environmentally Adaptive Autonomous Underwater Vehicle and Commu-
 650 nication,” IEEE Journal of Oceanic Engineering (accepted).
- 651 Brooke, J. (1981). “ARCS (Autonomous remotely controlled submersible),” in *Proceedings*
 652 *of the 1981 2nd International Symposium on Unmanned Untethered Submersible Technol-*
 653 *ogy*, IEEE, Vol. 2, p. 28.
- 654 Chassignet, E. P., Hurlburt, H. E., Smedstad, O. M., Halliwell, G. R., Hogan, P. J.,
 655 Wallcraft, A. J., Baraille, R., and Bleck, R. (2007). “The HYCOM HYbrid Coordinate
 656 Ocean Model data assimilative system,” Journal of Marine Systems **65**(1), 60–83, doi:
 657 [10.1016/j.jmarsys.2005.09.016](https://doi.org/10.1016/j.jmarsys.2005.09.016).
- 658 Chen, R., Poulsen, A., and Schmidt, H. (2019). “Spectral, spatial, and temporal character-
 659 istics of underwater ambient noise in the Beaufort Sea in 1994 and 2016,” The Journal of
 660 the Acoustical Society of America **145**(2), 605–614, doi: [10.1121/1.5088601](https://doi.org/10.1121/1.5088601).
- 661 Chen, R., and Schmidt, H. (2020). “Temporal and spatial characteristics of the Beaufort
 662 Sea ambient noise environment,” The Journal of the Acoustical Society of America **148**(6),
 663 3928–3941, doi: [10.1121/10.0002955](https://doi.org/10.1121/10.0002955).

- 664 Claus, B., Kepper, J. H., Suman, S., and Kinsey, J. C. (2018). “Closed-loop one-way-travel-
665 time navigation using low-grade odometry for autonomous underwater vehicles,” Journal
666 of Field Robotics **35**(4), 421–434, doi: [10.1002/rob.21746](https://doi.org/10.1002/rob.21746).
- 667 Deffenbaugh, M. (1997). “Optimal Ocean Acoustic Tomography and Navigation with Mov-
668 ing Sources,” Phd thesis.
- 669 Deffenbaugh, M., Bellingham, J. G., and Schmidt, H. (1996a). “The relationship between
670 spherical and hyperbolic positioning,” in *OCEANS 96 MTS/IEEE Conference Proceedings.*
671 *The Coastal Ocean - Prospects for the 21st Century*, Vol. 2, pp. 590–595, doi: [10.1109/OCEANS.1996.568293](https://doi.org/10.1109/OCEANS.1996.568293).
- 672 Deffenbaugh, M., Schmidt, H., and Bellingham, J. G. (1996b). “Acoustic positioning in a
673 fading multipath environment,” in *OCEANS 96 MTS/IEEE Conference Proceedings*, Vol.
674 2, pp. 596—600, doi: [10.1109/OCEANS.1996.568294](https://doi.org/10.1109/OCEANS.1996.568294).
- 675 Duda, T. F., Morozov, A. K., Howe, B. M., Brown, M. G., Speer, K., Lazarevich, P.,
676 Worcester, P. F., and Cornuelle, B. D. (2006). “Evaluation of a Long-Range Joint Acoustic
677 Navigation Thermometry System,” in *OCEANS 2006*, pp. 1–6, doi: [10.1109/OCEANS.2006.306999](https://doi.org/10.1109/OCEANS.2006.306999).
- 678 Duda, T. F., Zhang, W. G., and Lin, Y.-T. (2021). “Effects of Pacific Summer Water layer
679 variations and ice cover on Beaufort Sea underwater sound ducting,” J. Acoust. Soc. Am.
680 21.
- 681 Duda, T. F., Zhang, W. G., Lin, Y.-T., and Newhall, A. E. (2019). “Long-range sound
682 propagation in the Canada Basin,” .

- 685 Elisseeff, P., Schmidt, H., and Xu, W. (2002). “Ocean acoustic tomography as a data
686 assimilation problem,” IEEE Journal of Oceanic Engineering **27**(2), 275–282, doi: [10.1109/JOE.2002.1002482](https://doi.org/10.1109/JOE.2002.1002482).
- 687
- 688 Eustice, R. M., Whitcomb, L. L., Singh, H., and Grand, M. (2006). “Recent advances in
689 synchronous-clock one-way-travel-time acoustic navigation,” in *Oceans 2006*, IEEE, pp.
690 1–6, doi: [10.1109/OCEANS.2006.306931](https://doi.org/10.1109/OCEANS.2006.306931).
- 691 Eustice, R. M., Whitcomb, L. L., Singh, H., and Grund, M. (2007). “Experimental Re-
692 sults in Synchronous-Clock One-Way-Travel-Time Acoustic Navigation for Autonomous
693 Underwater Vehicles,” in *Proceedings 2007 IEEE International Conference on Robotics
and Automation*, pp. 4257–4264, doi: [10.1109/ROBOT.2007.364134](https://doi.org/10.1109/ROBOT.2007.364134).
- 694
- 695 Fossum, T. O., Norgren, P., Fer, I., Nilsen, F., Koenig, Z. C., and Ludvigsen, M. (2021).
696 “Adaptive Sampling of Surface Fronts in the Arctic Using an Autonomous Underwater
697 Vehicle,” IEEE Journal of Oceanic Engineering **46**(4), 1155–1164, doi: [10.1109/JOE.2021.3070912](https://doi.org/10.1109/JOE.2021.3070912).
- 698
- 699 Freitag, L., Ball, K., Partan, J., Koski, P., and Singh, S. (2016). “Long range acoustic com-
700 munications and navigation in the Arctic,” in *OCEANS 2015 - MTS/IEEE Washington*,
701 IEEE, pp. 1–5, doi: [10.23919/oceans.2015.7401956](https://doi.org/10.23919/oceans.2015.7401956).
- 702 Graupe, C. E., Van Uffelen, L. J., Webster, S. E., Worcester, P. F., and Dzieciuch, M. A.
703 (2019). “Preliminary results for glider localization in the Beaufort Duct using broadband
704 acoustic sources at long range,” in *OCEANS 2019 MTS/IEEE Seattle, OCEANS 2019*,
705 IEEE, pp. 1–6, doi: [10.23919/OCEANS40490.2019.8962637](https://doi.org/10.23919/OCEANS40490.2019.8962637).

- 706 Gwal, A., and Jain, A. (2011). “GPS scintillation studies in the arctic region during the
 707 first winter-phase 2008 Indian Arctic Expedition,” *Polar Science* **4**(4), 574–587, doi: [10.1016/j.polar.2010.08.001](https://doi.org/10.1016/j.polar.2010.08.001).
- 708
- 709 Hayes, D. R., and Morison, J. H. (2002). “Determining turbulent vertical velocity, and
 710 fluxes of heat and salt with an autonomous underwater vehicle,” *Journal of Atmospheric
 711 and Oceanic Technology* **19**(5), 759–779.
- 712 Howe, B. M., Miksis-Olds, J., Rehm, E., Sagen, H., Worcester, P. F., and Haralabus, G.
 713 (2019). “Observing the Oceans Acoustically,” *Frontiers in Marine Science* **6**(JUL), 1–22,
 714 doi: [10.3389/fmars.2019.00426](https://doi.org/10.3389/fmars.2019.00426).
- 715 Jackson, E. (1983). “Autonomous remotely controlled submersible ”ARCS”,” in *Proceedings
 716 of the 1983 3rd International Symposium on Unmanned Untethered Submersible Technol-
 717 ogy*, IEEE, Vol. 3, pp. 77–88.
- 718 Jakuba, M. V., Roman, C. N., Singh, H., Murphy, C., Kunz, C., Willis, C., Sato, T.,
 719 and Sohn, R. A. (2008). “Long-baseline acoustic navigation for under-ice autonomous
 720 underwater vehicle operations,” *Journal of Field Robotics* **25**(11-12), 861–879, doi: <https://doi.org/10.1002/rob.20250>.
- 721
- 722 Jung, T. S., Hegel, T. M., Bentzen, T. W., Egli, K., Jessup, L., Kienzler, M., Kuba, K.,
 723 Kukka, P. M., Russell, K., Suitor, M. P., and Tatsumi, K. (2018). “Accuracy and per-
 724 formance of low-feature GPS collars deployed on bison *Bison bison* and caribou *Rangifer
 725 tarandus*,” *Wildlife Biology* **2018**(1), doi: [10.2981/wlb.00404](https://doi.org/10.2981/wlb.00404).
- 726 Kepper, J. H., Claus, B. C., and Kinsey, J. C. (2017). “MEMS IMU and one-way-travel-
 727 time navigation for autonomous underwater vehicles,” in *OCEANS 2017 - Aberdeen*, IEEE,

- 728 Aberdeen, UK, pp. 1–9, doi: [10.1109/OCEANSE.2017.8084842](https://doi.org/10.1109/OCEANSE.2017.8084842).
- 729 Krishfield, R., Toole, J., Proshutinsky, A., and Timmermans, M. L. (2008). “Automated
 730 ice-tethered profilers for seawater observations under pack ice in all seasons,” *Journal of
 731 Atmospheric and Oceanic Technology* **25**(11), 2091–2105, doi: [10.1175/2008JTECH0587](https://doi.org/10.1175/2008JTECH0587).
- 732 [1](#).
- 733 Kukulya, A., Plueddemann, A., Austin, T., Stokey, R., Purcell, M., Allen, B., Littlefield, R.,
 734 Freitag, L., Koski, P., Gallimore, E., Kemp, J., Newhall, K., and Pietro, J. (2010). “Under-
 735 ice operations with a REMUS-100 AUV in the Arctic,” in *2010 IEEE/OES Autonomous
 736 Underwater Vehicles, AUV 2010*, IEEE, pp. 1–8, doi: [10.1109/AUV.2010.5779661](https://doi.org/10.1109/AUV.2010.5779661).
- 737 Kunz, C., Murphy, C., Camilli, R., Singh, H., Bailey, J., Eustice, R., Jakuba, M., Nakamura,
 738 K. I., Roman, C., Sato, T., Sohn, R. A., and Willis, C. (2008). “Deep sea underwater
 739 robotic exploration in the ice-covered arctic ocean with AUVs,” in *2008 IEEE/RSJ Inter-
 740 national Conference on Intelligent Robots and Systems, IROS*, IEEE, pp. 3654–3660, doi:
 741 [10.1109/IROS.2008.4651097](https://doi.org/10.1109/IROS.2008.4651097).
- 742 Light, R. D., and Morison, J. (1989). “The Autonomous Conductivity-Temperture Vehicle:
 743 First in the Seashuttle Family of Autonomous Underwater Vehicle’s for Scientific Pay-
 744 loads,” in *Proceedings OCEANS*, Vol. 3, pp. 793–798, doi: [10.1109/OCEANS.1989.586683](https://doi.org/10.1109/OCEANS.1989.586683).
- 745 Litvak, A. G. (2015). “Acoustics of the deepwater part of the Arctic Ocean and of Russia’s
 746 Arctic shelf,” *Herald of the Russian Academy of Sciences* **85**(3), 239–250, doi: [10.1134/S1019331615030144](https://doi.org/10.1134/S1019331615030144).
- 747 Mikhalevsky, P. N., Sperry, B. J., Woolfe, K. F., Dzieciuch, M. A., and Worcester, P. F.
 748 (2020). “Deep ocean long range underwater navigation,” *The Journal of the Acoustical
 749 Society of America* **147**(4), 1–10, doi: [10.1121/10.3.2019-0001](https://doi.org/10.1121/10.3.2019-0001).

- 750 Society of America **147**(4), 2365–2382, doi: [10.1121/10.0001081](https://doi.org/10.1121/10.0001081).
- 751 National Research Council (**2011**). *National Security Implications of Climate Change for*
752 *U.S. Naval Forces* (National Academies Press, Washington, D.C.).
- 753 Norgren, P., Lubbad, R., and Skjetne, R. (**2014**). “Unmanned underwater vehicles in Arctic
754 operations,” in *Proceedings of the 22nd IAHR International Symposium on Ice. Singapore*,
755 pp. 89–101.
- 756 Paull, L., Saeedi, S., Seto, M., and Li, H. (**2014**). *AUV Navigation and Localization: A*
757 *Review*, **39**, pp. 131–149.
- 758 Plueddemann, A. J., Kukulya, A. L., Stokey, R., and Freitag, L. (**2012**). “Autonomous
759 Underwater Vehicle Operations Beneath Coastal Sea Ice,” IEEE/ASME Transactions on
760 Mechatronics **17**(1), 54–64, doi: [10.1109/TMECH.2011.2174798](https://doi.org/10.1109/TMECH.2011.2174798).
- 761 Porter, M. B. (**2011**). “The bellhop manual and user’s guide: Preliminary draft,” .
- 762 Poulsen, A. J., and Schmidt, H. (**2017**). “Acoustic noise properties in the rapidly changing
763 Arctic Ocean,” Proceedings of Meetings on Acoustics (28), 1–10, doi: [10.1121/2.0000552](https://doi.org/10.1121/2.0000552).
- 764 Randeni, S., Schneider, T., and Schmidt, H. (**2020**). “Construction of a high-resolution
765 under-ice AUV navigation framework using a multidisciplinary virtual environment,” in
766 *2020 IEEE/OES Autonomous Underwater Vehicles Symposium, AUV 2020*, IEEE, pp.
767 1–7, doi: [10.1109/AUV50043.2020.9267950](https://doi.org/10.1109/AUV50043.2020.9267950).
- 768 Randeni, S., Schneider, T., Schmidt, H., Bhatt, E., and Viquez, O. (**2021**). “A high-
769 resolution AUV navigation framework with integrated communication and tracking for
770 under-ice deployments,” Field Robotics (in review).

- 771 Reid, T., Walter, T., Blanch, J., and Enge, P. (2016). “GNSS Integrity in The Arctic,”
772 Navigation **63**(4), 469–492, doi: [10.1002/navi.169](https://doi.org/10.1002/navi.169).
- 773 Rossby, T., Dorson, D., and Fontaine, J. (1986). “The RAFOS System,” Journal of
774 Atmospheric and Oceanic Technology **3**(4), 672–679, doi: [10.1175/1520-0426\(1986\)
775 003<0672:TRS>2.0.CO;2](https://doi.org/10.1175/1520-0426(1986)003<0672:TRS>2.0.CO;2).
- 776 Rypkema, N. R., Fischell, E. M., and Schmidt, H. (2017). “One-Way Travel-Time Inverted
777 Ultra-Short Basline Localization for Low-Cost Autonomous Underwater Vehicles,” in *2017*
778 *IEEE International Conference on Robotics and Automation*, Singapore, pp. 4920–4926.
- 779 Schmidt, H., and Schneider, T. (2016). “Acoustic communication and navigation in the
780 new Arctic — A model case for environmental adaptation,” 2016 IEEE Third Underwa-
781 ter Communications and Networking Conference (UComms) 1–4, doi: [10.1109/UComms.
782 2016.7583469](https://doi.org/10.1109/UComms.2016.7583469).
- 783 Schneider, T., Petillo, S., Schmidt, H., and Murphy, C. (2015). “The dynamic compact
784 control language version 3,” in *OCEANS 2015-Genova*, IEEE, pp. 1–7.
- 785 Schneider, T., and Schmidt, H. (2010). “Unified command and control for heterogeneous
786 marine sensing networks,” Journal of Field Robotics **27**(6), 876–889, doi: [https://doi.
787 org/10.1002/rob.20346](https://doi.org/10.1002/rob.20346).
- 788 Schneider, T., and Schmidt, H. (2018). “NETSIM: A Realtime Virtual Ocean Hardware-in-
789 the-loop Acoustic Modem Network Simulator,” in *2018 Fourth Underwater Communica-
790 tions and Networking Conference (UComms)*, IEEE, pp. 1–5, doi: [10.1109/UComms.2018.
791 8493188](https://doi.org/10.1109/UComms.2018.8493188).

- 792 Schneider, T., Schmidt, H., and Randeni, S. (2021). “Self-Adapting Under-Ice Integrated
 793 Communications and Navigation Network,” 2021 Fifth Underwater Communications and
 794 Networking Conference (UComms) 1–5, doi: [10.1109/UComms50339.2021.9598012](https://doi.org/10.1109/UComms50339.2021.9598012).
- 795 Singh, S., Grand, M., Bingham, B., Eustice, R., Singh, H., and Freitag, L. (2006). “Un-
 796 derwater acoustic navigation with the WHOI Micro-Modem,” in *Oceans 2006*, IEEE, pp.
 797 1–4, doi: [10.1109/OCEANS.2006.306853](https://doi.org/10.1109/OCEANS.2006.306853).
- 798 Swanlund, D., Maraj, R., Schuurman, N., Hope, R., Donkers, K., Aquin, M., and Rickerby,
 799 G. (2016). “Gps performance in yukon’s arctic coast,” *Geografiska Annaler: Series A,*
 800 *Physical Geography* **98**(4), 361–368, doi: [10.1111/geoa.12143](https://doi.org/10.1111/geoa.12143).
- 801 Themens, D. R., Jayachandran, P. T., and Langley, R. B. (2015). “The nature of GPS
 802 differential receiver bias variability: An examination in the polar cap region,” *Journal of*
 803 *Geophysical Research: Space Physics* **120**(9), 8155–8175, doi: [10.1002/2015JA021639](https://doi.org/10.1002/2015JA021639).
- 804 Timmermans, M.-L., and Winsor, P. (2013). “Scales of horizontal density structure in the
 805 Chukchi Sea surface layer,” *Continental Shelf Research* **52**, 39–45.
- 806 Toole, J., Krishfield, R., Timmermans, M.-L., and Proshutinsky, A. (2011). “The Ice-
 807 Tethered Profiler: Argo of the Arctic,” *Oceanography* **24**(3), 126–135, doi: [10.5670/oceanog.2011.64](https://doi.org/10.5670/oceanog.2011.64).
- 808 Van Uffelen, L. J., Howe, B. M., Nosal, E. M., Carter, G. S., Worcester, P. F., and Dzieci-
 809 uch, M. A. (2016). “Localization and subsurface position error estimation of gliders using
 810 broadband acoustic signals at long range,” *IEEE Journal of Oceanic Engineering* **41**(3),
 811 501–508, doi: [10.1109/JOE.2015.2479016](https://doi.org/10.1109/JOE.2015.2479016).

- 813 Van Uffelen, L. J., Nosal, E.-M., Howe, B. M., Carter, G. S., Worcester, P. F., Dzieciuch,
 814 M. A., Heaney, K. D., Campbell, R. L., and Cross, P. S. (2013). “Estimating uncertainty
 815 in subsurface glider position using transmissions from fixed acoustic tomography sources,”
 816 The Journal of the Acoustical Society of America **134**(4), 3260–3271, doi: [10.1121/1.4818841](https://doi.org/10.1121/1.4818841).
- 818 Van Uffelen, L. J. V. (2021). “Global Positioning Systems: Over Land and Under Sea,”
 819 Acoustics Today **17**(1), 9.
- 820 Webster, S. E., Eustice, R. M., Singh, H., and Whitcomb, L. L. (2009). “Preliminary
 821 deep water results in single-beacon one-way-travel-time acoustic navigation for underwater
 822 vehicles,” in *2009 IEEE/RSJ International Conference on Intelligent Robots and Systems,*
 823 *IROS 2009*, IEEE, pp. 2053–2060, doi: [10.1109/IROS.2009.5354457](https://doi.org/10.1109/IROS.2009.5354457).
- 824 Webster, S. E., Eustice, R. M., Singh, H., and Whitcomb, L. L. (2012). “Advances in single-
 825 beacon one-way-travel-time acoustic navigation for underwater vehicles,” The International
 826 Journal of Robotics Research **31**(8), 935–950, doi: [10.1177/0278364912446166](https://doi.org/10.1177/0278364912446166).
- 827 Webster, S. E., Freitag, L. E., Lee, C. M., and Gobat, J. I. (2015). “Towards real-time
 828 under-ice acoustic navigation at mesoscale ranges,” in *Proceedings - IEEE International*
 829 *Conference on Robotics and Automation*, IEEE, Vol. 2015-June, pp. 537–544, doi: [10.1109/ICRA.2015.7139231](https://doi.org/10.1109/ICRA.2015.7139231).
- 831 Wu, M., Barmin, M. P., Andrew, R. K., Weichman, P. B., White, A. W., Lavelly, E. M.,
 832 Dzieciuch, M. A., Mercer, J. A., Worcester, P. F., and Ritzwoller, M. H. (2019). “Deep
 833 water acoustic range estimation based on an ocean general circulation model: Application
 834 to PhilSea10 data,” The Journal of the Acoustical Society of America **146**(6), 4754–4773,

835 doi: [10.1121/1.5138606](https://doi.org/10.1121/1.5138606).